

# Two decades of distributed global radiation time series across a mountainous semiarid area (Sierra Nevada, Spain)

Cristina Aguilar<sup>1</sup>, Rafael Pimentel<sup>1</sup>, María J. Polo<sup>1</sup>

<sup>1</sup>Fluvial Dynamics and Hydrology Research Group, Andalusian Institute of Earth System Research, University of Cordoba, Cordoba, Spain

*Correspondence to:* Cristina Aguilar (caguilar@uco.es)

**Abstract.** The main drawback of the reconstruction of high resolution distributed global radiation ( $R_g$ ) time series in mountainous semiarid environments is the common lack of station-based solar radiation registers. This work presents nineteen years (2000-2018) of high spatial resolution (30 m) daily, monthly, and annual global radiation maps derived using the GIS-based model proposed by Aguilar et al. (2010) in a mountainous area in southern Europe: Sierra Nevada (SN) Mountain Range (Spain). The model was driven by in situ daily global radiation measurements, from sixteen weather stations with historical records in the area, a 30 m digital elevation model and 240 cloud-free Landsat images. The applicability of the modeling scheme was validated against daily global radiation records at the weather stations. Mean RMSE values of  $2.63 \text{ MJ m}^{-2} \text{ day}^{-1}$  and best estimations on clear-sky days were obtained. Daily  $R_g$  at weather stations revealed greater variations in the maximum values but no clear trends with altitude in any of the statistics. However, at the monthly and annual scales, there is an increase in the high extreme statistics with the altitude of the weather station, especially above 1500 m a.s.l. Monthly  $R_g$  maps showed significant spatial differences of up to  $200 \text{ MJ m}^{-2} \text{ month}^{-1}$  that clearly followed the terrain configuration. July and December were clearly the months with the highest and lowest values of  $R_g$  received and the highest scatter in the monthly  $R_g$  values was found in the spring and fall months. The monthly  $R_g$  distribution was highly variable along the study period (2000-2018). Such variability, especially in the wet season (October-May), determined the inter annual differences of up to  $800 \text{ MJ m}^{-2} \text{ year}^{-1}$  in the incoming global radiation in SN. The time series of the surface global radiation datasets here provided can be used to analyze inter-annual and seasonal variation characteristics of the global radiation received in SN with high spatial detail (30 m). They can also be used as cross-validation reference data for other global radiation distributed datasets generated in SN with different spatio-temporal interpolation techniques. Daily, monthly, and annual datasets in this study are available at <https://doi.pangaea.de/10.1594/PANGAEA.921012> (Aguilar et al., 2021).

## 1 Introduction

High mountain areas in semiarid environments present singular characteristics due to the continuous interaction of alpine conditions in the summits with the surrounding semiarid climate. They play a key role as water providers during the warm and dry season when they often constitute the only water source for many rivers. Here, water fluxes from the snowpacks show a shift from the predominant partition between snowmelt and sublimation usually found in colder and wetter climates on an annual and seasonal basis (Herrero and Polo, 2016). This shift is caused by the radiation balance that enhances sublimation during cold and dry periods and intense snowmelt rates during late winter and spring in these areas (McDonnell et al., 2013; Liu et al., 2019). However, weather stations are not always equipped to monitor the global radiation nor their components and, moreover, they are seldom found in high altitudes, especially over 1500 m a.s.l., which makes it difficult to accurately assess not only the solar radiation temporal regime but also the spatial patterns of solar radiation fields in high mountain areas. This impacts the availability of data for studies in mountains dealing with climate and hydrology, global warming, ecosystem services provided by the snow areas, and environmental and social and economic impacts on-site and downstream (Yang et al., 2010; Liu et al., 2012a; Tang et al., 2019). It is not surprising that many mountain regions are identified as biodiversity hotspots around the world, with Mediterranean and other semiarid to arid regions being highly represented (Myers et al., 2000; O'Farrell et al., 2010; Hewitt, 2011; Pauli et al., 2012).

There are several research papers on solar radiation estimations from routine ground-based observations in high altitude regions (Dubayah and van Katwijk, 1992; Dubayah, 1994; Tovar et al., 1995; Oliphant et al., 2003; Tovar-Pescador et al., 2006; Yang et al., 2006, 2010; Batllés et al., 2008; Bosch et al., 2008; Sheng et al., 2009; Aguilar et al., 2010; Mamassis et al., 2012; Chen et al., 2013; Zhang et al., 2020). All of them insist on the need to consider topographic effects and advise of the errors that simple interpolation/extrapolation techniques can create. Radiation data obtained from a dense and properly-maintained weather station network in mountainous areas are rarely available and therefore, modeling techniques need to be applied. Liu et al. (2012a) state that the most difficult issue in solar radiation modeling in data sparse regions is cloud accounting, due to the rapid spatially and temporally changing weather conditions and the three-dimensional structure of clouds. This complexity adds to the heterogeneity resulting from shadowing and reflection due to steep topography (Dubayah, 1992; Batllés et al., 2008; Mamassis et al., 2012; Chen et al., 2013; Zhang et al., 2019, 2020).

According to Dubayah and Rich (1995), as solar radiation models become more complex, they can be more difficult to use, mainly because of the requirement for additional input data. In fact, the complexity of physically-based solar radiation formulations for topography and the lack of the data needed to drive such formulations led in the past to the lack of suitable modeling tools (Dubayah, 1994). Thus, it is important that the models allow for some flexibility regarding the component of radiation calculated and the input data needed.

Excluding traditional interpolation methods there are two major methods for solar radiation modeling, namely, satellite-derived solar radiation estimates, and Geographic Information Systems (GIS)-based solar radiation models. Satellite-derived solar radiation models provide a wide spatial and temporal coverage, but low spatial resolution when dealing with pixels with a

63 strong topographic gradient. By contrast, GIS-based models calculate the incoming solar radiation for each cell of a digital  
64 elevation model (DEM) and allow for higher spatial resolutions including topographic effects. In the past decades, several  
65 models based on GIS have been proposed (e.g., Dubayah and Rich, 1995; Fu and Rich, 2000a, 2002; Wilson and Gallant,  
66 2000; Goldberg and Häntzschel, 2002; Sùri and Hofierka, 2004; Liu et al., 2012a; Zhang et al., 2019, 2020). Required input  
67 data include digital elevation values and atmospheric attenuation parameters that are commonly estimated from ground-based  
68 measurements and/or satellite data (Dubayah, 1994).

69 The aim of this study was to generate the spatiotemporal distribution of global solar radiation in a high mountain semiarid area  
70 in southern Spain with a modeling scheme that reconstructs time map series from the usually available weather datasets. For  
71 this purpose, a GIS-based topographic solar radiation model (Aguilar et al., 2010) was applied in Sierra Nevada (SN) (Spain),  
72 a high mountain range running west-east parallel to the Mediterranean coastline with influence from both the sea and the  
73 African continent to the South, and the continental conditions to the North. The accuracy of solar radiation estimates by the  
74 model were evaluated in terms of the error in the approximation to observed data. This study site is a high-value environmental  
75 area declared Biosphere Reserve by UNESCO in 1986 due to the exceptional presence of endemisms (Heywood, 1995; Blanca  
76 et al., 1998; Anderson et al., 2011; Cañadas et al., 2014). Besides, SN is also included in the Global Change Observatories  
77 Network given its singular location between two seas and two continents, and its extreme topographic gradients (Bonet-García  
78 et al., 2015).

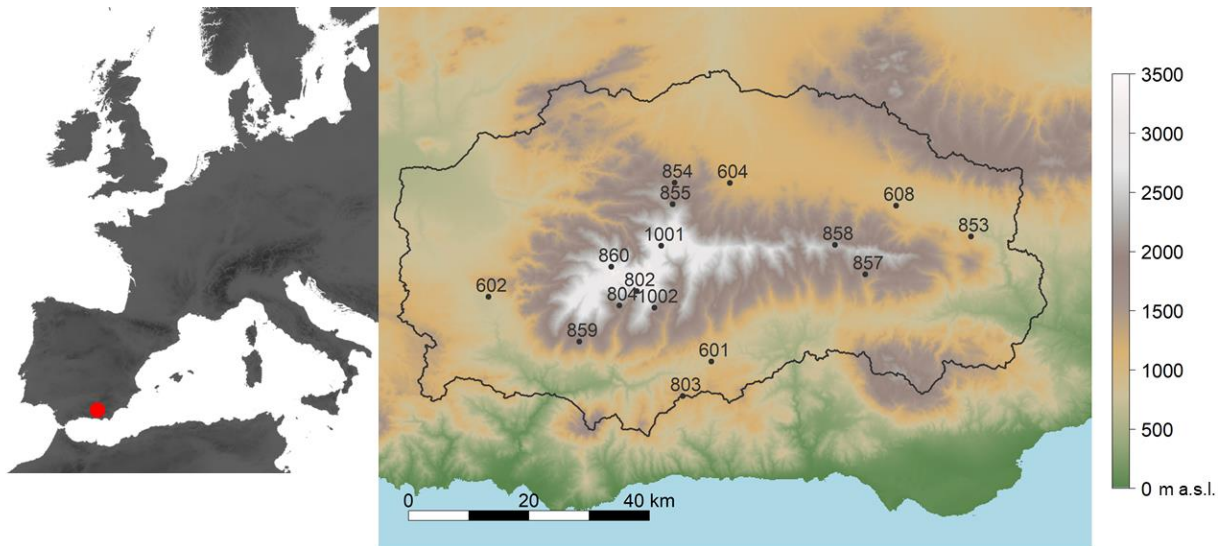
79 This paper presents 19 years of daily, monthly, and annual solar radiation maps with high resolution (30 m) over SN. The huge  
80 number of members involved in the management of this area make this information valuable in different fields, such as:  
81 hydrology, crucial role of energy budget in the hydrological cycle over this area; ecology, ecological communities' behaviour  
82 and development clearly link with the amount of energy available; production systems downstream, as hydropower facilities  
83 and traditional to tropical crop systems from the top to downhill. Besides, these data sets directly contribute, or are relevant  
84 for many studies that could do so, to two of the 23 Unsolved Problems in Hydrology (UPH) recently posed by Blöschl et al.  
85 (2019) in a participatory analytical discussion among the scientific community: UPH 16 “How can we use innovative  
86 technologies to measure surface and subsurface properties, states and fluxes at a range of spatial and temporal scales?” and  
87 UPH 5 “What causes spatial heterogeneity and homogeneity in runoff, evaporation, subsurface water and material fluxes  
88 (carbon and other nutrients, sediments), and in their sensitivity to their controls (e.g. snowfall regime, aridity, reaction  
89 coefficients)?”.

## 90 **2 Study site**

91 The Sierra Nevada mountain range (SN) is located 35 km north from the Mediterranean Sea (Fig. 1) and constitutes a  
92 mountainous area of the Natura 2000 network. Elevations rise up from 262 m a.s.l. to 3479 m a.s.l. in a 4583.72 km<sup>2</sup> area that  
93 runs parallel to the sea. High altitudinal gradients are representative of the area, with variation in elevation of about 3400 m in  
94 less than 40 km of horizontal distance and a mountain climate in the summits surrounded by Mediterranean climate in the

95 lower areas. Thus, the interaction of such conditions creates a strong heterogeneity in terms of soil types, landforms and  
96 vegetation species that determine a complex hydrological response in the area and many endemic species (Heywood, 1995;  
97 Blanca et al., 1998; Anderson et al., 2011). The rainfall regime is highly variable, even in consecutive years, with annual  
98 cumulative values in the period (1960-2000) that range between 200 mm in dry years to 1000 mm in wet years, with an average  
99 value of 510 mm (Pérez-Palazón et al., 2015). Temperature regime is also heterogeneous, with values of 26, 12.5 and 0.4 °C,  
100 for maximum, mean, and minimum daily temperature in the same period.

101 The snow presence becomes relevant from November above 2000 m a.s.l. and extends up to spring with conditions that make  
102 it possible the activity of a major ski resort in the area. However, in some winters, mild episodes can be found in January and  
103 February that melt most of the snow much earlier than the mean end of the snow season in the area (Herrero et al., 2009;  
104 Herrero and Polo, 2012). Because of its singular characteristics and fragile environment, Sierra Nevada receives international  
105 recognition as a Biosphere Reserve (1986), a National Park (1999), an Important Bird Area (2003), a Special Area of  
106 Conservation (2012) and one of the International Global Change Observatories in Mountain Areas. These environmental  
107 protection figures together with the different and numerous members involved in the management of such a unique area have  
108 determined the strong effort in data collection in the last years to advance in the knowledge of the different aspects that  
109 determine the dynamics of this natural system. Moreover, global warming impacts threaten the environmental values of this  
110 system but also the associated ecosystem services and social and economic activities due to the estimated shift of the snowfall  
111 regime (Pérez-Palazón et al., 2018).



112  
113 **Figure 1. Location of the study site in southern Spain (left). Digital Elevation Model (DEM) and weather stations in Sierra Nevada**  
114 **(SN) (right). The numbers correspond to the station codes.**

### 3 Data

#### 3.1 Input data

A digital elevation model (DEM) with 30 m spatial resolution and 1m vertical precision was used in this study (Fig. 1). The DEM was provided by the Andalusian regional administration and it was generated by digital stereo correlation of aerial photographs of the Spanish National Plan of Orthophotography. The DEM is used to calculate the slope, aspect, sky view factor and terrain configuration maps that are used in the modeling process (Dozier and Frew, 1990).

Meteorological input data are the longest available in-situ daily global radiation ( $R_{go}$ ) of 16 weather stations over the area (Fig. 1 and Table 1). The extent of the records in all weather stations ( $N_o$  in Table 1) was considered long enough to carry out the evaluation process dating from February 2000 for the oldest station (608 in Table 1). 12 out of the 16 weather stations are located above 1500 m a.s.l. and 7 of them above 2000 m a.s.l. (Fig. 1). The stations belong to four different organizations: The Department of Agriculture, Fisheries and Environment of the Andalusian Government (601-608 in Table 1), the Water and Environment Agency (1001 and 1002 in Table 1), the National Parks Organization (853-860 in Table 1) and the Guadalfeo Network (802-804 in Table 1) described in Polo et al. (2019). Pyranometers used to collect the data were of different natures but all of them with a characteristic range of around  $0.35 \sim 1.1 \mu\text{m}$ : Skye SP1110 (stations 601, 602, 604 and 608), Kipp & Zonen SP-Lite pyranometer (station 802), HuksefluxLP02 (station 803), HuksefluxNR01 (stations 1001, 1002 and 804) and Middleton Net Solar CNR1 (stations 853, 854, 855, 857, 858, 859 and 860).

In order to generate the complete global radiation data series for the whole-time span (01/02/2000-31/12/2018) we first apply a quality-control check to the recorded data at the weather stations.

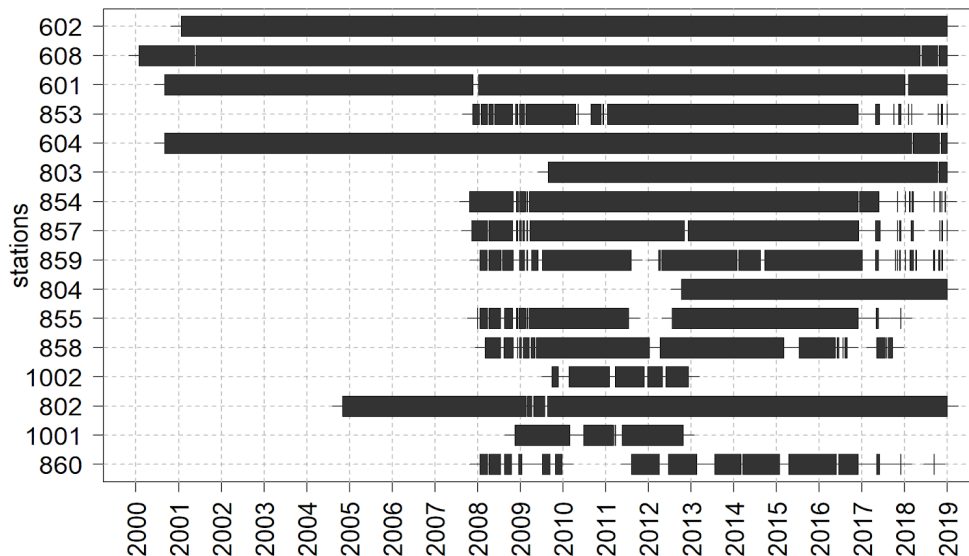
#### 3.2 Data quality control

Numerous studies on quality control of measured solar radiation data can be found in the literature (Geiger et al., 2002; Younes et al., 2005; Moradi, 2009; Journée and Bertrand, 2011). Compared to other meteorological variables, solar radiation measurement is more prone to errors (Moradi, 2009). Younes et al. (2005) state two main sources of errors related to in situ measurement of solar radiation: those related to equipment and uncertainty and operational errors. Thus, prior to any computation two basic screenings were applied to recorded daily global radiation data to discard suspicious records associated with equipment and operational errors (Younes et al., 2005).

1. Observed daily global radiation ( $R_{go}$ ) must be between the daily extraterrestrial radiation ( $R_{ext}$ ) and a minimum 3% of  $R_{ext}$  (Geiger et al., 2002; Moradi, 2009).
2. Observed daily global radiation ( $R_{go}$ ) must be lower than the clear daily global radiation ( $R_{gcs}$ ) observed under a highly transparent clear sky (Wu et al., 2007).  $R_{gcs}$  values were calculated with the model developed by Ineichen and Perez (2002) and the parameterization of Kasten and Young (1989) for the air mass. More detail regarding the equation as well as its parameters can be found in Aguilar et al. (2010).

The excluded values from these tests did not reach 1% of the data at any weather station.

147 A third quality control screening was applied following Younes et al. (2005) to detect erroneous data due to operational errors  
 148 related with particularities of weather stations in high altitudes (e.g., shadows, impacts of snow, mechanical failures, etc.).  
 149 They suggest a semi-automatic procedure that allows the creation of an expectancy envelope in the clearness index (CI)-diffuse  
 150 to global irradiance ratio ( $k$ ) domain to reject data too obviously erroneous. The CI data range is divided into bands of equal  
 151 width, within which the mean and standard deviation of the  $k$  values,  $\mu_k$  and  $\sigma_k$ , are calculated. The top and bottom boundary  
 152 shapes are identified by fitting two polynomials through the points  $\mu_k \pm b\sigma_k$  limited between 0 and 1 to respect the physical  
 153 range of the CI. In this study  $b$  values between 2 and 3 were applied in order to limit both, the rejection of good data and the  
 154 acceptance of erroneous data to small percentages.  
 155 The CI was calculated with the observed data at each weather station. However, no measurements of daily diffuse radiation,  
 156  $R_d$ , were available. Thus, the model proposed by Aguilar et al. (2010) was applied to generate daily diffuse radiation ( $R_{dp}$ ) at  
 157 each weather station without considering the observed global data at such station. Obviously, this assumption depends on the  
 158 validity of the model as well as on the quality of  $R_{go}$  datasets at the remaining weather stations. However, under the common  
 159 lack of diffuse solar radiation measurements like the present one, modeling them can be an alternative (e.g., Yang et al., 2020)  
 160 to reject erroneous  $R_g$  observations. This approach was proposed once the model had already been validated in a previous study  
 161 (Aguilar et al., 2010) but keeping in mind the intrinsic limitations and assumptions previously stated.  
 162 After this quality test, the percentage of excluded values did not reach 10% at any weather station, with a mean value close to  
 163 2% when the whole set of stations was considered. Table 1 shows selected descriptors of the data sets at each station in this  
 164 study after all the quality check process and Figure 2 shows the chronogram of the final input data availability per station (N  
 165 in Table 1) used in this study.



166  
 167 **Figure 2. Data availability in the analyzed period (01 Feb 2000 - 31 Dec 2018) for each weather station. Stations are sorted by**  
 168 **increasing altitude from the top to the bottom row.**

**Table 1.** Information of the weather stations included in this study: elevation,  $z$  (m a.s.l.); code; data length, as initial and final dates of the time series; number of initially available daily records,  $N_o$  (days); number of available daily records after the quality check,  $N$  (days); rate of days for cloudy,  $N_{CI<0.3}$  (%), partially cloudy,  $N_{0.3<CI<0.6}$  (%), and clear-sky conditions,  $N_{CI>0.6}$  (%); and maximum,  $R_{go\_max}$  ( $MJ\ m^{-2}\ day^{-1}$ ), mean,  $R_{go\_mean}$  ( $MJ\ m^{-2}\ day^{-1}$ ), and minimum,  $R_{go\_min}$  ( $MJ\ m^{-2}\ day^{-1}$ ), daily global radiation observed values. The selected descriptors for sky conditions and global radiation correspond to registered data after quality check.

$z$	Code	Initial date	Final date	$N_o$	$N$	$N_{CI<0.3}$	$N_{0.6<CI<0.3}$	$N_{CI>0.6}$	$R_{go\_max}$	$R_{go\_mean}$	$R_{go\_min}$
781	602	26/01/2001	31/12/2018	6521	6370	8	23	69	33.80	18.49	0.80
942	608	01/02/2000	31/12/2018	6883	6686	6	26	68	34.20	18.83	0.70
950	601	05/09/2000	31/12/2018	6600	6449	7	27	66	33.00	18.17	0.60
975	853	21/11/2007	29/12/2018	2833	2827	8	30	62	32.37	18.01	1.00
1212	604	05/09/2000	31/12/2018	6665	6485	7	29	64	33.00	18.09	0.70
1332	803	27/08/2009	31/12/2018	3407	3282	7	22	71	33.41	18.95	0.71
1530	854	26/10/2007	16/12/2018	3176	3169	10	28	62	32.91	17.97	1.10
1732	857	16/11/2007	29/12/2018	3042	3034	11	25	64	32.84	18.31	0.81
1735	859	23/01/2008	21/11/2018	2577	2573	11	23	66	33.67	19.11	0.59
2141	804	10/10/2012	31/12/2018	2272	2206	7	21	72	33.91	19.05	0.82
2155	855	02/01/2008	30/11/2017	2522	2519	13	30	57	33.64	17.64	0.78
2300	858	09/03/2008	20/09/2017	2385	2380	12	28	60	34.58	17.99	0.99
2325	1002	15/11/2008	29/10/2012	951	951	8	22	70	35.60	20.47	1.55
2510	802	04/11/2004	31/12/2018	5050	4849	6	19	75	36.29	20.28	0.69
2867	1001	16/11/2007	01/01/2014	1071	1071	6	28	66	33.70	18.06	1.68
3097	860	23/01/2008	09/09/2018	1858	1705	13	25	62	35.79	18.20	1.12

174

175 **3.3 Generation of global radiation maps**

176 The GIS-based solar radiation model proposed by Aguilar et al. (2010) that was previously implemented and validated in a  
177 small subwatershed located in the southwest of Sierra Nevada (Fig. 1) was extended to the whole area in this study. For  
178 validation purposes, data registered at weather stations are considered to represent the average values of the 30 m cell of the  
179 DEM on which they are located (Batllés et al., 2008; Martínez-Durbán et al., 2009).

180 The main equations and flowchart of the model are shown in Appendix A. The complete explanation of the algorithms as well  
181 as the justification of the assumptions of the model can be found in detail in Aguilar et al. (2010).

182 The model was developed to be run using limited data but considering the agents that constitute the main sources of the spatial  
183 and temporal variability of solar radiation. Results generated by the model include hourly maps of diffuse, beam and reflected  
184 solar radiation values with minimum input data requirements as only topographic data, albedo estimations and measured daily  
185 global radiation records ( $R_{go}$ ) at least at one weather station are required. As for the daily global radiation registers, even when

they are missing, their estimation from other more readily available meteorological data could always be a choice from the literature (Hargreaves and Samani, 1982; Bristow and Campbell, 1984; Allen, 1997; Bechini et al., 2000; Winslow et al., 2001; Donatelli et al., 2003, 2006; Yang and Koike, 2005; Diodato and Bellocchi, 2007; Wu et al., 2007; Ruiz-Arias et al., 2011; Liu et al., 2012b; El Ouderni et al., 2013; Mullen et al., 2013).

The generation of global radiation maps with the model applied (Aguilar et al., 2010) requires a proper characterization of the spatio-temporal patterns of albedo in the study site. 240 cloud-free Landsat imagery available for the study period from Landsat 5 TM (49 images), Landsat 7 ETM+ (141 images) and Landsat 8 OLI (50 images) with a 30 m spatial resolution were used. Figure 3 shows the specific dates and sensors of the 240 images analyzed in this study. All images were first properly corrected, and their reflectivity values computed (Pimentel et al., 2014). Albedo was then derived for each image following the same procedure applied in Aguilar et al. (2010), which is based on the methodology described by Brest and Goward (1987), and linearly interpolated on a daily time scale for the whole study period.

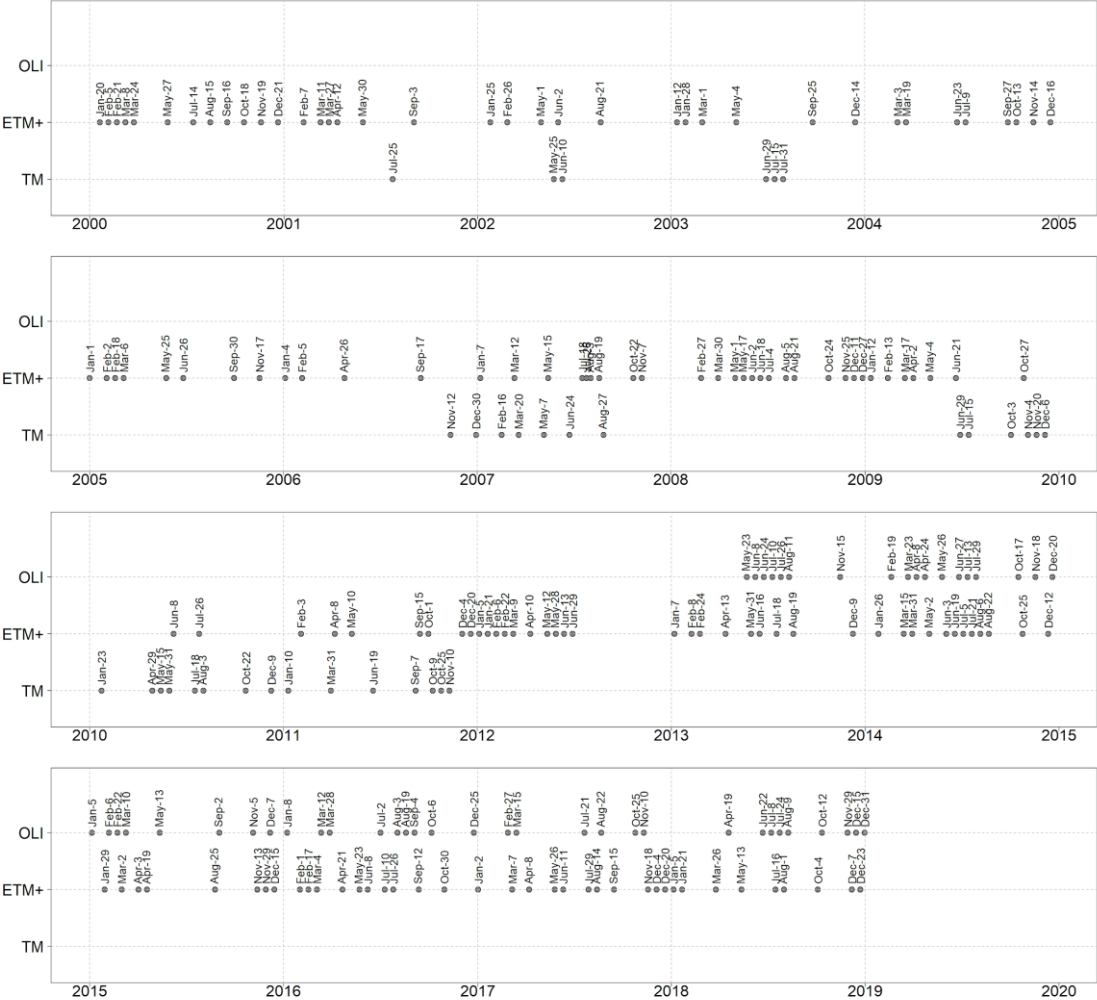


**Figure 3. Dates and sensors of each Landsat image analyzed in the study period (01 Feb 2000 - 31 Dec 2018).**



### 3.4 Cross-validation at weather stations

Once daily global radiation estimates were generated by the model a cross validation was applied at each weather station on the daily scale. This was carried out on a leave-one-out process, i.e., data from a weather station were removed from the input dataset to the model and predicted values ( $R_{gp}$ ) at that weather station were then compared to observed data ( $R_{go}$ ).

Different indicators were computed to quantitatively evaluate the performance of the model (Muneer et al., 2007):

-The Root Mean Square Error (RMSE) (Eq. 1), where  $R_{gp}$  and  $R_{go}$  are the predicted and observed daily global radiation ( $\text{MJ m}^{-2} \text{ day}^{-1}$ ), respectively, and  $N$  is the number of observed daily data. It measures the difference between values predicted by the model and those which were actually observed.

$$RMSE = \sqrt{\frac{\sum (R_{gp} - R_{go})^2}{N}} \quad (1)$$

-The deviation from the 1:1 line of observed vs. predicted daily solar radiation values. Linear fits forced through the origin were obtained (Eq. 2) and the slopes ( $\alpha$  in Eq. 2) are desired to be equal to 1. The coefficient of determination,  $R^2$ , as the ratio of the explained variation to the total variation, was also computed.

$$R_{gp} = \alpha \cdot R_{go} \quad (2)$$

The RMSE values and linear fits were obtained for the whole dataset at each weather station, and also for different cloudiness levels to consider different atmospheric states that may condition the performance of the model according to previous studies (Batllés et al., 2008; Martínez-Durbán et al., 2009; Ruiz-Arias et al., 2009). Based on the cloudiness three types of weather conditions were analyzed: cloudy days ( $CI < 0.3$ ), partly cloudy days ( $0.3 \leq CI < 0.6$ ) and clear-sky days or cloudless days ( $CI \geq 0.6$ ).

The cross-validation assessment is summarized in Figure 4. With the global datasets (in black in Fig. 4), a very close approximation of the model estimates to recorded data was obtained (mean  $\alpha$  value of 0.98 and mean  $R^2$  values of 0.91). RMSE values varied for the different stations and ranged from 1.81 (station 804) to 3.76 (station 860) with a mean value of  $2.63 \text{ MJ m}^{-2} \text{ day}^{-1}$ .

When the analysis was carried out in terms of the cloudiness level, a general overestimation by the model (e.g., a mean  $\alpha$  value of 1.41) was always seen on cloudy days ( $CI \leq 0.3$ ). In contrast, on clear-sky days ( $CI > 0.6$ ) slopes were very close to 1 with a mean  $\alpha$  value of 0.96. An intermediate behavior was found on partly cloudy days ( $0.3 < CI \leq 0.6$ ) when the model slightly under predicted (e.g., stations 854 and 608) or over predicted depending on the weather station. As for RMSE values, the lowest values were always found for clear sky days, when the cloud influence is minimal and the attenuation is mostly explained by changes in the atmospheric transmittance, followed by partly cloudy days with mean values of  $2.07$  and  $3.07 \text{ MJ m}^{-2} \text{ day}^{-1}$ , respectively. The highest RMSE values were always found on cloudy days with mean values of  $3.70 \text{ MJ m}^{-2} \text{ day}^{-1}$ . The high proportion of clear-sky days (65%) and the low RMSE values on these days ( $2.07 \text{ MJ m}^{-2} \text{ day}^{-1}$ ) revealed the general good agreement of the model estimates with observed data. This is especially important in semiarid environments, where energy-

230 limited hydrological processes (e.g., soil moisture depletion, evaporation, or snowmelt) are more relevant on clear-sky days  
 231 and they must be carefully computed in water and energy balance modeling, irrigation scheduling, etc. (Chen et al., 1999;  
 232 Mamassis et al., 2012).  
 233 There is no clear pattern in the errors obtained with the elevation of the stations. The goodness of the model estimates was  
 234 more affected by the interaction of the different characteristics of the weather station (e.g., slope, aspect, surrounding terrain  
 235 configuration, orographic effects in the vertical development of clouds, etc.) than by the height of the station itself.  
 236 To validate the modeling scheme applied, another well-known GIS-based solar radiation model, Solar Analyst (SA) (Fu and  
 237 Rich, 2000b) was also applied in the study site. Error values in the approximation to observed data and linear fits obtained in  
 238 SN are shown in Appendix B. In view of the errors obtained with SA estimates (Table B.1) we can select the modeling scheme  
 239 here proposed (Subsection 3.3) over SA to analyze the spatial and temporal behavior of solar radiation in SN.  
 240 The errors obtained in Figure 4 were within the order of magnitude of those found in previous studies in other mountainous  
 241 areas (Yang et al., 2006; 2010; Zhang et al., 2020) and slightly improved those previously obtained on a small subarea (10 x 5  
 242 km<sup>2</sup>) in the north-eastern side of SN. Here, Tovar-Pescador et al. (2006) analyzed the application of SA in clear sky days with  
 243 a 168 global radiation dataset from 14 weather stations located at between 1091 and 1659 m.a.s.l. They obtained R<sup>2</sup> values of  
 244 0.75, similar to the value here obtained with SA estimates in the whole SN area (0.77 in Table B.1) but lower than the R<sup>2</sup> equal  
 245 to 0.99 obtained with the model (in orange in Figure 3). Then, Batllés et al. (2008) in another application of SA in the same  
 246 area with a 2-year daily dataset obtained the best performances for clear-sky days. RMSE values obtained in clear-sky days in  
 247 the present study, of 11.1 % (2.07 MJ m<sup>-2</sup> day<sup>-1</sup>); were the same as those obtained by Batllés et al. (2008) for clear sky days  
 248 (11%). Later, Ruiz-Arias et al. (2009) evaluated the application of four different GIS-based solar radiation models with a 523  
 249 global radiation dataset at the same study site. RMSE values for the global dataset ranged between 1.99 and 7.28 MJ m<sup>-2</sup> day<sup>-1</sup>  
 250 <sup>1</sup> depending on the model.  
 251 The order of magnitude of the errors (Figure 4) and its comparison with those obtained with more computationally and data  
 252 demanding GIS-based models in previous studies let us to conclude that the model is the best choice to generate global radiation  
 253 data series in SN.  
 254 Therefore, once the model was validated in the study site, daily R<sub>g</sub> maps were generated and aggregated at the monthly and  
 255 annual scales.

256

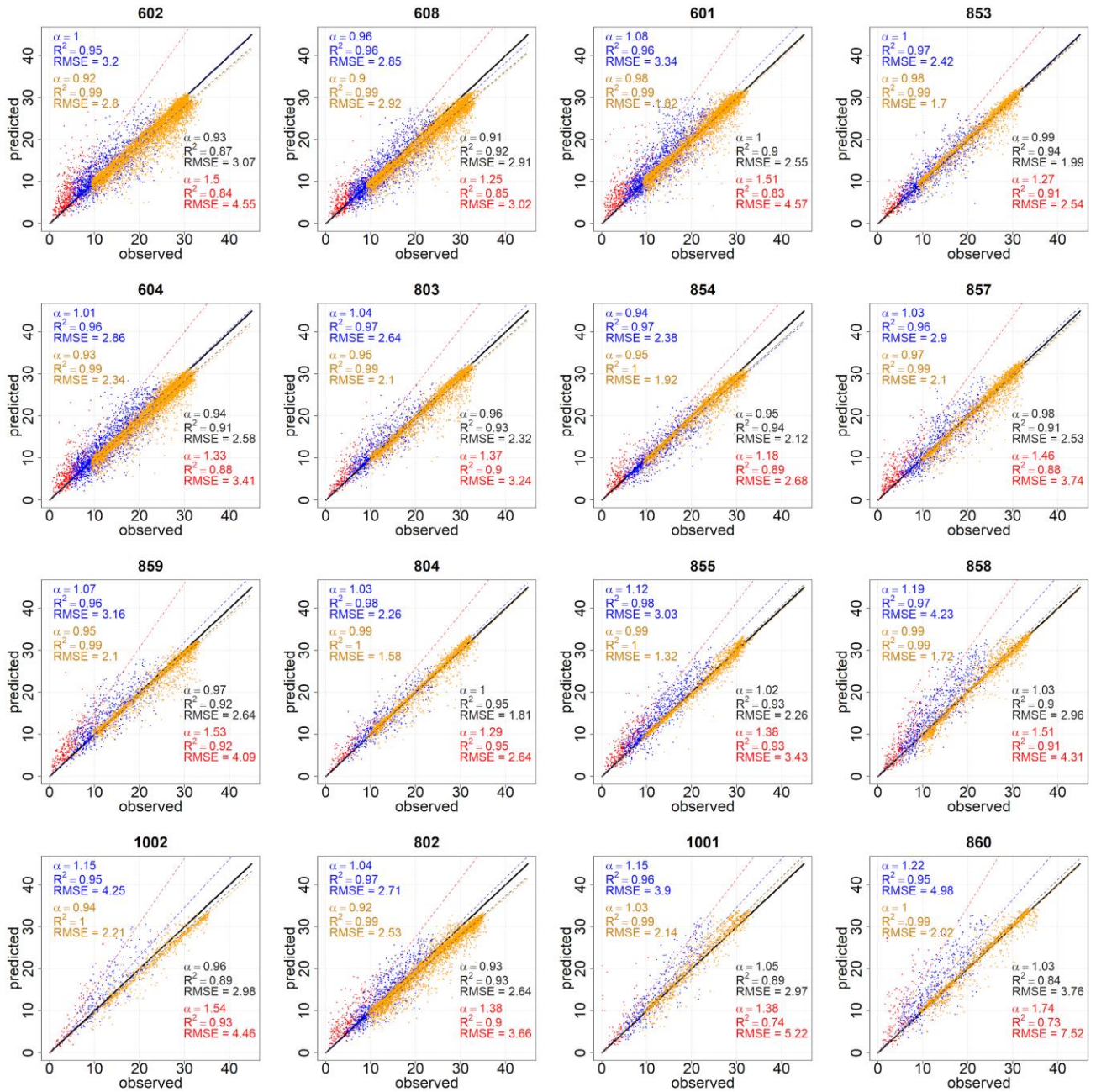


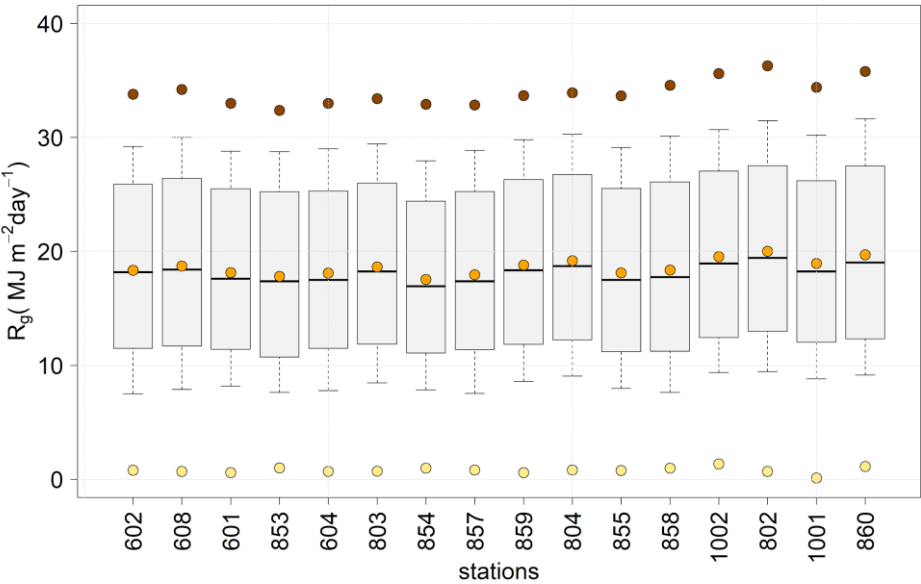
**Figure 4. Cross validation analysis. Linear fits of daily predicted vs. observed  $R_g$  (MJ m<sup>-2</sup> day<sup>-1</sup>) at each of the selected stations for the global data (black), cloudy (CI<0.3 - red), partly cloudy (0.3<CI<0.6 - blue) and clear-sky days (CI>0.6 - orange). Stations are sorted by increasing altitude from left to right and from the top to the bottom row.**

264 **4 Results**

265 Daily, monthly, and annual  $R_g$  datasets in SN are analyzed in this section at two spatial scales. First, the results at the weather  
266 station scale are presented. Thus, possible relationships between altitude and/or location of the weather station with the  
267 different  $R_g$  statistics and how this relation changes with the temporal scale of analysis can be assessed. Then, the  $R_g$  maps that  
268 can be downloaded as specified in section 6 are analyzed.

269 **4.1 Daily time series of global radiation in Sierra Nevada**

270 Figure 5 shows the statistical distribution of the daily  $R_g$  at each weather station ordered by increasing altitude and illustrates  
271 several questions. First, there is a very similar interquartile range among stations. Second, there are greater variations in the  
272 maximum daily  $R_g$  among the different stations with a mean value of  $34.0 \text{ MJ m}^{-2} \text{ day}^{-1}$ . Third, even though a slight increase  
273 with altitude can be shown in the high extreme statistics of the daily  $R_g$  values (e.g., in the maximum or in the 90<sup>th</sup> percentile),  
274 there is not a clear trend. Therefore, other factors such as orientation, proximity to the sea or the terrain configuration in the  
275 surrounding terrain as suggested by Batllés et al. (2008) constitute relevant features in the study site.  
276 Figure 6 shows an example of the spatial distribution in three representative days of cloudy, partially cloudy, and clear-sky  
277 conditions. Here the spatial distribution is clearly influenced by the topography of SN, especially in the clear sky day.



278  
279 **Figure 5. Statistical distribution of daily  $R_g$  ( $\text{MJ m}^{-2} \text{ day}^{-1}$ ) time series at each of the selected stations over the study area. The box**  
280 **shows 50% of the data, delimited by Q1 (lower) and Q3 (upper), the solid line represents the median, and whiskers show 10<sup>th</sup> and**  
281 **90<sup>th</sup> percentiles. Brown, orange and yellow dots represent daily maximum, mean and minimum time series values. Stations are sorted**  
282 **by increasing altitude from left to right.**

283

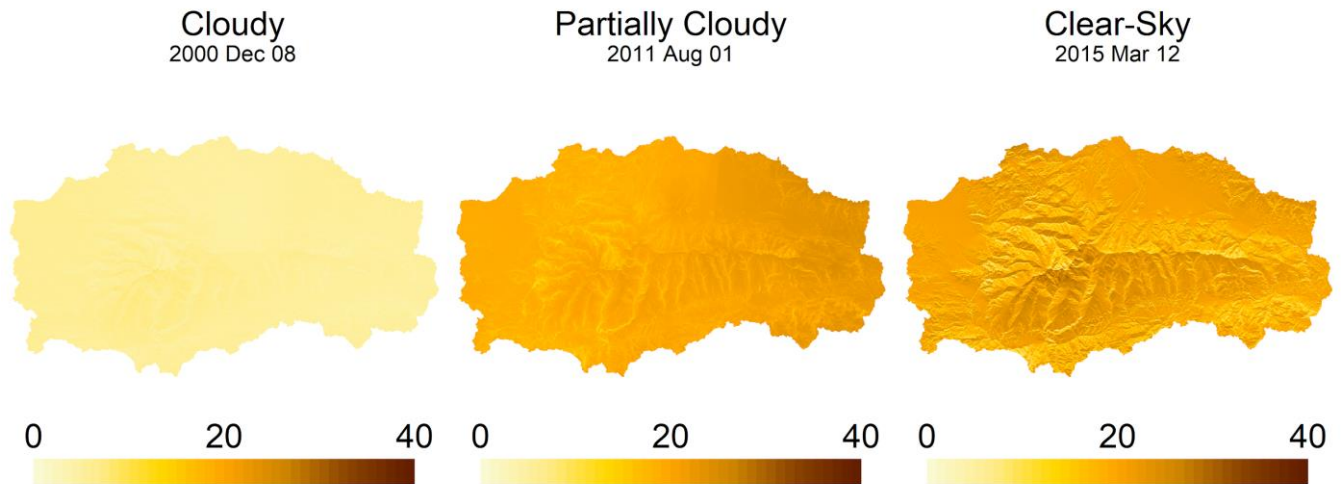


**Figure 6. Daily  $R_g$  ( $\text{MJ m}^{-2} \text{ day}^{-1}$ ) in SN for three selected days that represent the three levels of cloudiness considered in this study: cloudy, partially cloudy and clear-sky.**

#### 4.2 Monthly time series of global radiation in Sierra Nevada

The statistical distribution of monthly  $R_g$  per weather station (Fig. 7) shows that in every station: i) July and December constitute the months with the highest and the lowest values of  $R_g$ , respectively; ii) there is a quite linear increase in the monthly  $R_g$  values from January to July and a sudden drop in August with a slightly convex evolution till December; and iii) the interquartile range is significantly higher in the spring and fall, than in the summer and winter months.

The increase in the high extreme statistics of radiation with the altitude of the weather station becomes more apparent at the monthly scale (Fig. 7) than at the daily scale (Fig. 5) previously analyzed. Thus, maximum values of around  $1000 \text{ MJ m}^{-2} \text{ month}^{-1}$  are reached in July in the highest stations (e.g. 1002, 802, 1001 and 860 in Fig. 7) whereas this value decreases to around  $910 \text{ MJ m}^{-2} \text{ month}^{-1}$  in the four lowest stations with the exception of station 608.

Monthly  $R_g$  maps show significant spatial differences of up to  $200 \text{ MJ m}^{-2} \text{ month}^{-1}$  in both the mean monthly values (Fig. 8) that clearly follow the terrain configuration with summits and valleys receiving high and low solar radiation values, respectively. For example, the area in the north of SN that is highly shadowed by the highest peaks in the Iberian Peninsula (Mulhacen and Veleta with 3482 and 3396 m a.s.l., respectively) is easily visible, with the lowest relative levels of insolation received within SN especially in the summer months (June, July and August in Fig. 8).

Both, maps of the monthly mean and standard deviation of  $R_g$  (Fig. 8) and the statistical distribution of the monthly  $R_g$  in the study site (Fig. 9), show the same behaviour as the one obtained at the weather stations regarding: i) July and December as the months with the highest and lowest values of  $R_g$  received in SN; and ii) the highest scatter in the monthly  $R_g$  values in the spring and fall months.

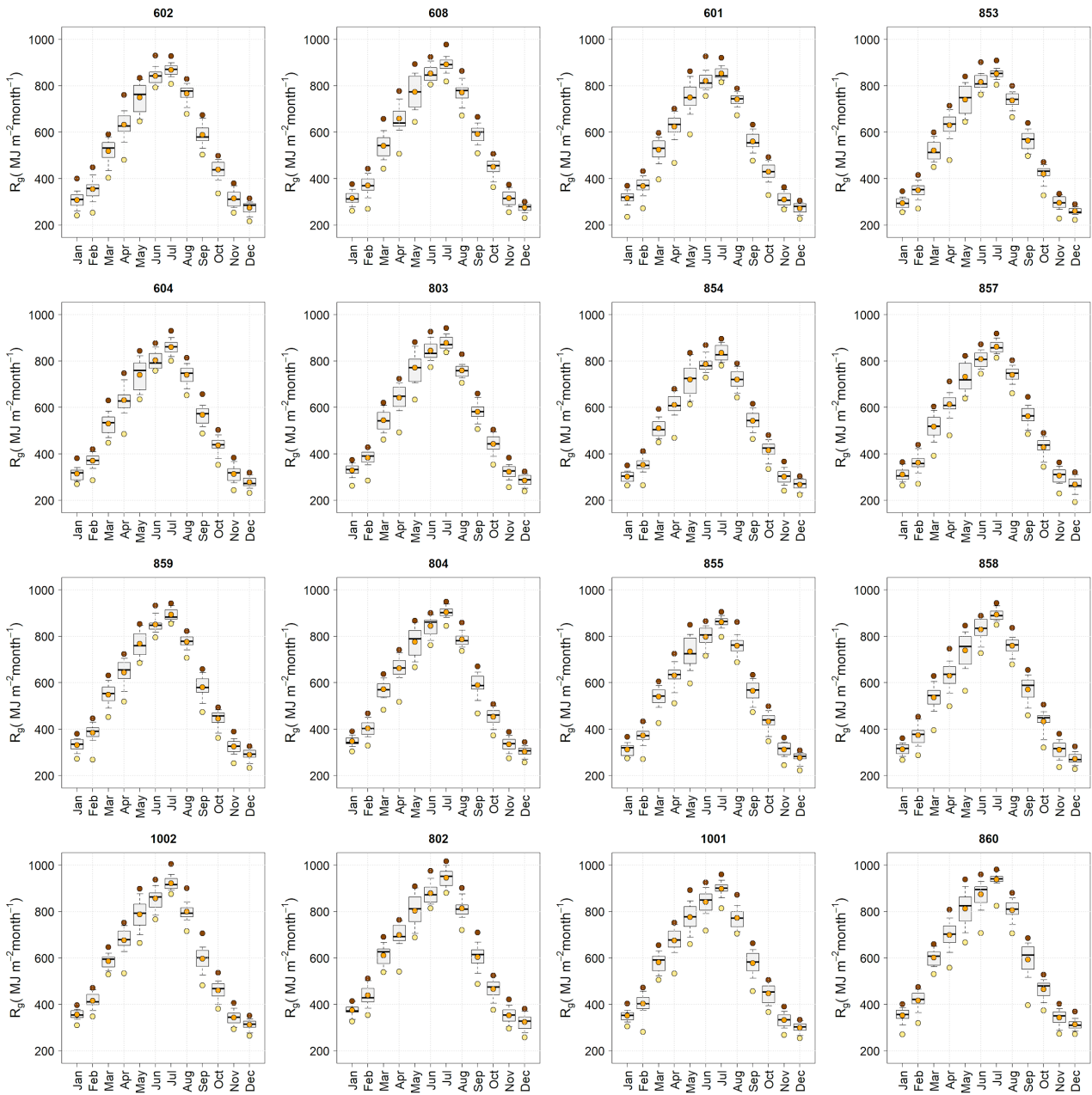
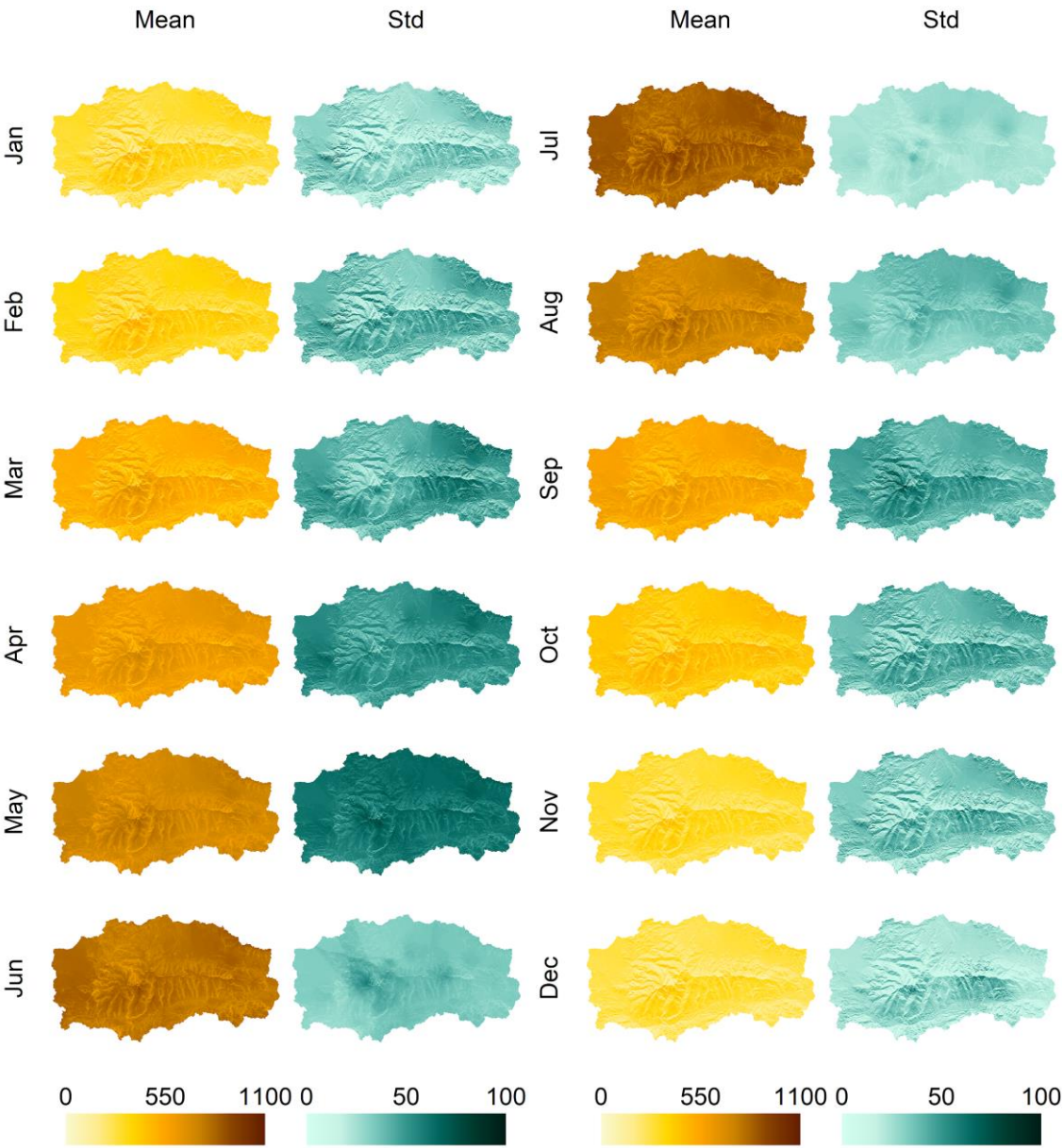


**Figure 7. Statistical distribution of monthly  $R_g$  ( $\text{MJ m}^{-2} \text{month}^{-1}$ ) time series at each of the selected stations over the study area. The box shows 50% of the data, delimited by Q1 (lower) and Q3 (upper), the solid line represents the median, and whiskers show 10<sup>th</sup> and 90<sup>th</sup> percentiles. Brown, orange and yellow dots represent monthly maximum, mean and minimum time series values. Stations are sorted by increasing altitude from left to right and from the top to the bottom row.**





314

315 **Figure 8. Monthly average and standard deviation of  $R_g$  ( $\text{MJ m}^{-2} \text{ month}^{-1}$ ) in the study period (2000-2018) in SN.**

316

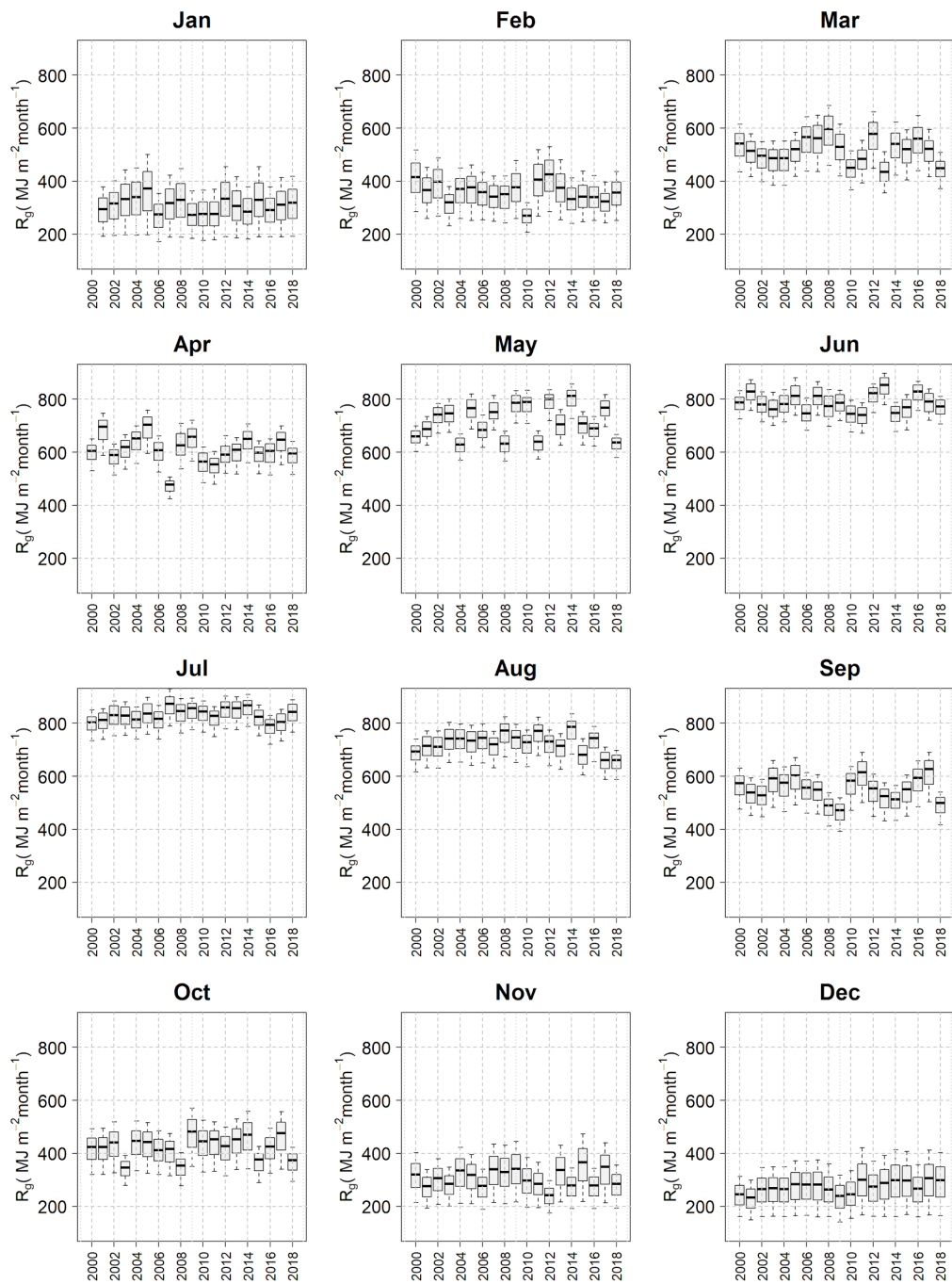


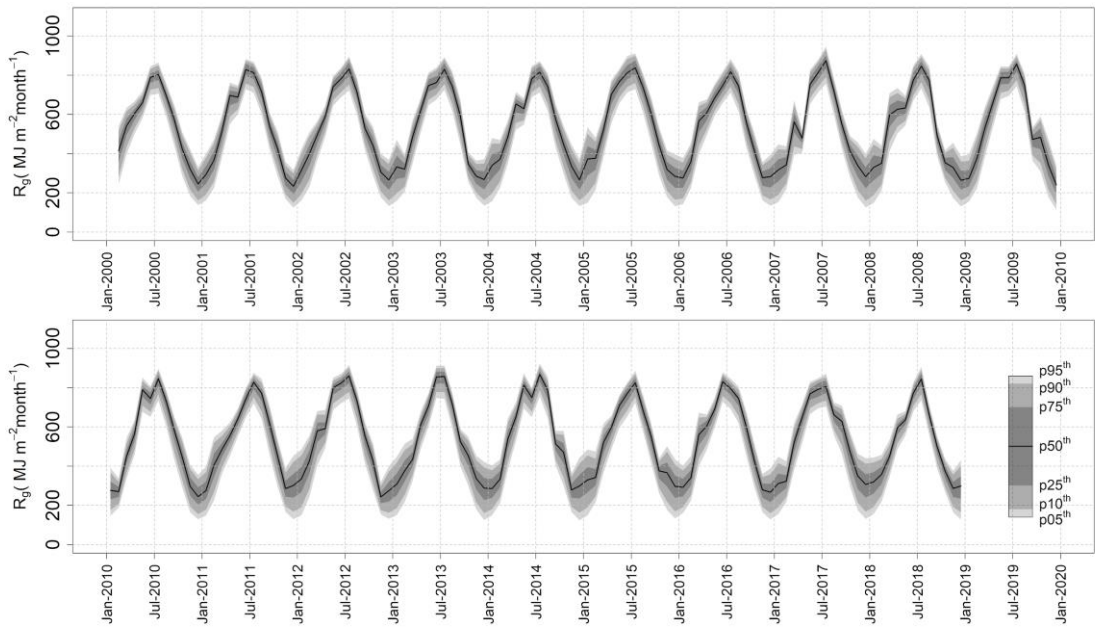
**Figure 9. Statistical distribution of the monthly  $R_g$  (MJ m<sup>-2</sup> month<sup>-1</sup>) values throughout the study area. Whisker boxes represent the 10<sup>th</sup>, 25<sup>th</sup>, 50<sup>th</sup>, 75<sup>th</sup> and 90<sup>th</sup> percentiles of each monthly map per year**



For the study period (2000-2018), there is a great heterogeneity in the statistical distribution of the monthly  $R_g$  in the study site (Fig. 9) especially in the incoming radiation along the months of the wet season (October-May). In this way, in the most insolated years in the study period (2005 and 2012), significantly higher monthly radiation values were found in certain months of the springtime (March and May 2012 and April 2005). In those months, the higher than usual rate of clear-sky over cloudy days finally determines the annual differences in the incoming global radiation in SN.

When considering the temporal evolution of the distribution of  $R_g$  within the monthly maps in SN (Fig. 10), certain interannual differences can be observed along the study period, such as the existence of certain months in spring with unexpected low monthly radiation values (eg. 2001, 2004, 2007 and 2008), or two relative maximum monthly  $R_g$  values (e.g. 2009, 2010 and 2014). Moreover, Figure 10 shows a higher scatter in the monthly maximum (June-August) and minimum (November-January)  $R_g$  values in SN than when the analysis is carried out at each weather station (Fig. 7).

331



332

333 **Figure 10. Evolution of the statistical distribution of monthly  $R_g$  ( $\text{MJ m}^{-2} \text{ month}^{-1}$ ) in the study period (2001-2018) throughout the**  
 334 **study area. Grayscale colours represent the following percentiles: 5<sup>th</sup>, 10<sup>th</sup>, 25<sup>th</sup>, 50<sup>th</sup>, 75<sup>th</sup>, 90<sup>th</sup> and 95<sup>th</sup>.**

### 335 4.3 Annual times series of global radiation in Sierra Nevada

336 Unlike at the daily scale (Fig. 5), a great variability among the different weather stations in terms of the global radiation  
 337 received at the annual temporal scale is found (Fig. 11). Thus, we find minimum annual  $R_g$  values from  $5920 \text{ MJ m}^{-2} \text{ year}^{-1}$  in  
 338 station 854 to around  $6750 \text{ MJ m}^{-2} \text{ year}^{-1}$  in station 1002. This difference is even bigger in the maximum annual  $R_g$  values from  
 339  $6700$  to  $7720 \text{ MJ m}^{-2} \text{ year}^{-1}$  in stations 854 and 802, respectively, and is also shown in the interquartile range.

When analyzing the influence of altitude, the weather stations above 1500 m a.s.l (854, 857, 859, 804, 855, 858, 1002, 802, 1001, 860 in Fig. 11) show their altitudinal gradient in all the statistics of the annual  $R_g$  values considered. Annual  $R_g$  maps (Fig. 12) show the same spatial differences that follow the terrain configuration as those observed in the monthly time series (Fig. 8). For example, the area in the north of SN that is highly shadowed as previously mentioned corresponds to the area with the mean minimum annual values received in the study period, 4063 MJ m<sup>-2</sup> year<sup>-1</sup>, that only represents 63% the mean annual accumulated values in SN (6316 MJ m<sup>-2</sup> year<sup>-1</sup>).

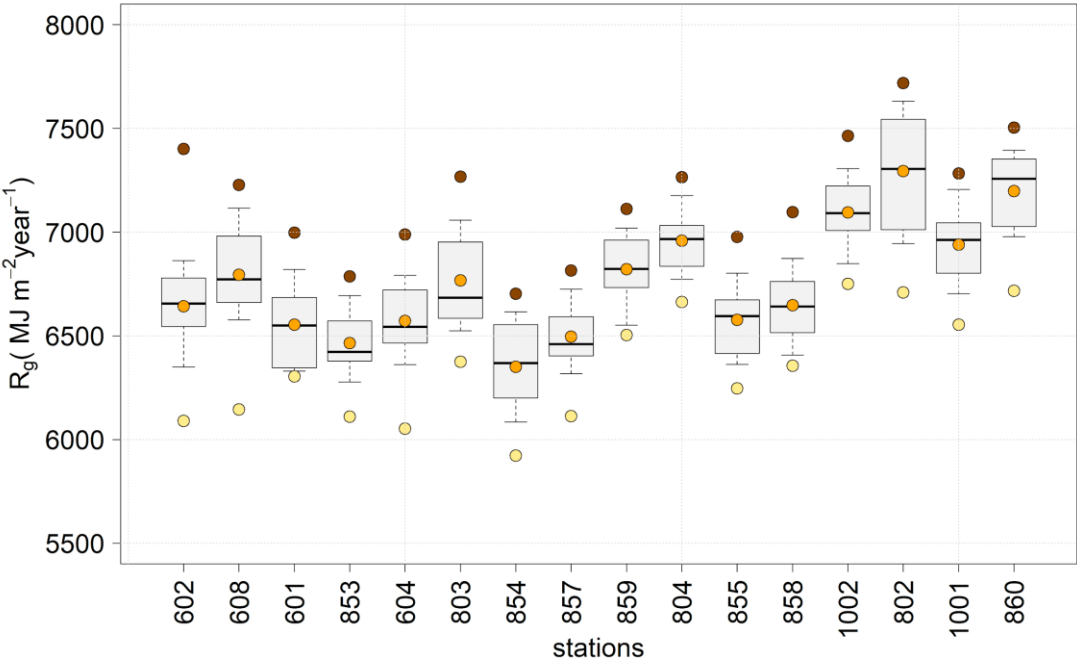


**Figure 11. Statistical distribution of annual  $R_g$  (MJ m<sup>-2</sup> year<sup>-1</sup>) time series at each of the selected stations over the study area. The box shows 50% of the data, delimited by Q1 (lower) and Q3 (upper), the solid line represents the median, and whiskers show 10<sup>th</sup> and 90<sup>th</sup> percentiles. Brown, orange and yellow dots represent annual maximum, mean and minimum time series value. Stations are sorted by increasing altitude from left to right.**

Significant interannual differences can be easily shown with differences in the mean annual  $R_g$  value in the study area of up to 800 MJ m<sup>-2</sup> year<sup>-1</sup> between 2005 and 2018. Such years with particularly high and low annual incoming radiation also presented higher (6800 MJ m<sup>-2</sup> year<sup>-1</sup>) and lower median annual  $R_g$  values (6200 MJ m<sup>-2</sup> year<sup>-1</sup>), respectively, than the annual median for the whole study period in SN (6456 MJ m<sup>-2</sup> year<sup>-1</sup>) (Fig. 13). These results agree with the annual irradiation map obtained by Batllés et al. (2008) in the north-eastern part of SN. They reported maximum and minimum annual values of 7516 and 2342 MJ m<sup>-2</sup> year<sup>-1</sup> on the summits and in deep valleys, respectively, and thus, concluded that irradiation levels were more related to topographic characteristics than to altitude.

1500 5500 9500



Figure 12. Annual global radiation ( $\text{MJ m}^{-2} \text{ year}^{-1}$ ) in the study period (2001-2018) in SN.

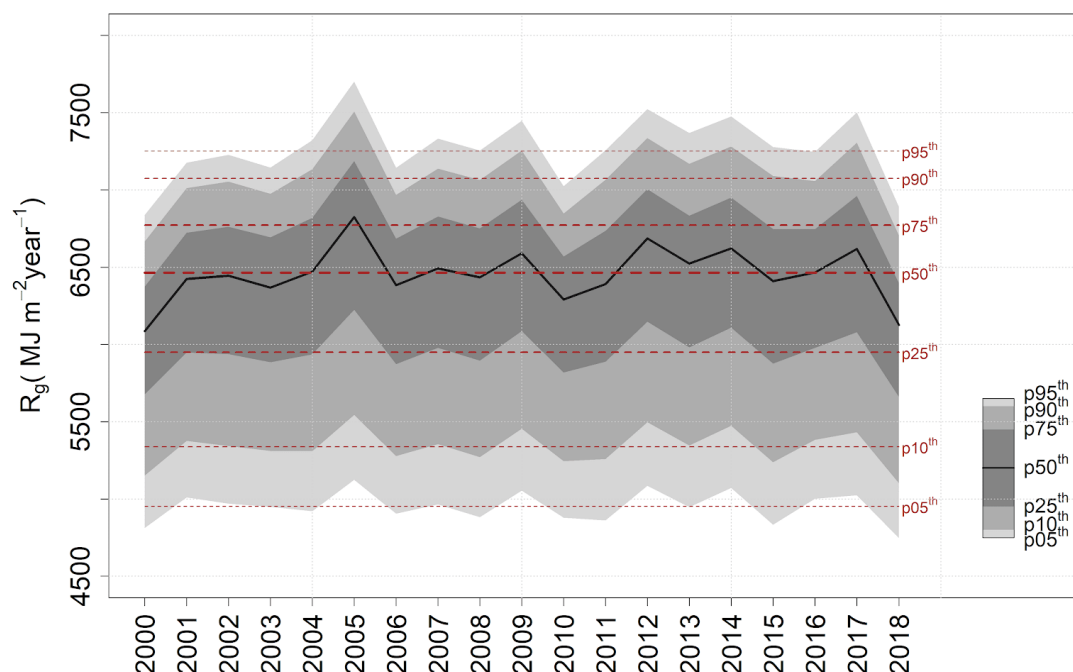


**Figure 13. Evolution of the statistical distribution of annual  $R_g$  ( $\text{MJ m}^{-2} \text{year}^{-1}$ ) in the study period (2001-2018) throughout the study area. Dashed lines represent the mean values of the percentiles analyzed.**

## 5 Data availability

The daily, monthly and annual global radiation maps derived in this study can be accessed and downloaded in.ncdf format from: <https://doi.pangaea.de/10.1594/PANGAEA.921012> (Aguilar et al., 2021). Besides, a .txt file containing the availability (code 1) or gaps (code 0) in the daily  $R_g$  observations at each weather station has been added as a supplement to this paper. Hourly datasets were also computed in this study but due to their large storing capacity requirements they have not been included in the data repository specified above. Thus, hourly maps can be provided for certain dates upon request to the authors. However, a validation of these hourly datasets like the one applied in the daily estimates at the weather stations has not been specifically carried out in this study. Therefore, in case hourly maps are requested to the authors, these data should be taken with caution as the only available validation in SN was carried out at one weather station (802 in Fig. 1) and for a shorter period (2004-2010) in Aguilar et al. (2010).

## 6 Final remarks

This study presents nineteen years (2000-2018) of daily, monthly, and annual global radiation maps of high spatial resolution (30 m) in a high mountain Mediterranean site. In these areas the common lack of weather stations in high altitudes makes it difficult to accurately assess solar radiation spatial patterns.

A GIS-based modelling scheme based on measurements or estimations of incoming daily global radiation was applied and validated in the sixteen weather stations available at this unique study site. Mean RMSE values ranged from 1.81 to 3.76 MJ m<sup>-2</sup> day<sup>-1</sup>, depending on the weather station. The best estimations were always obtained on clear-sky days, when mean RMSE values decreased to 2.07 MJ m<sup>-2</sup> day<sup>-1</sup>. The largest errors were obtained on cloudy days, which constitute on average 10% of the daily datasets, and, therefore, future research should be conducted in order to improve the estimations in these situations keeping the minimum input data requirements (daily global radiation data) advantage of the model. However, the high proportion (65%) of clear-sky days, and the low RMSE values on those days, allow one to conclude that there is a good agreement between the model estimates and observed data in the study site.

Spatial differences of around 2000 MJ m<sup>-2</sup> yr<sup>-1</sup> were found within each year analyzed. In addition, significant differences were easily shown between the years in mean incoming values of up to 800 MJ m<sup>-2</sup> yr<sup>-1</sup>. Those differences were mostly due to the variability in the incoming radiation at the wet season (October-May), with higher rates of clear-sky days in the most insolated years (e.g., 2005).

Thus, we can affirm that the modeling scheme here applied is an efficient option in semiarid mountainous areas, where daily global radiation datasets constitute the only source of solar radiation data.

Time series of these surface global radiation datasets can be used to analyze inter-annual and seasonal variation characteristics of the global radiation received in SN with high spatial detail (30 m). The availability of long global radiation datasets allows to capture the annual variability within each cycle of the Sun activity, as reported in the literature (Scaffetta and Wilson, 2013), and thus estimate its contribution to the annual variability of other climate variables in these semiarid mountainous areas.

Dense and properly-maintained weather station networks in mountainous areas are rarely available. Thus, these datasets can also be used as cross-validation reference data for other global radiation distributed datasets generated in SN with different spatio-temporal interpolation techniques.

These results can also assess the order of magnitude of different sources of spatial variability (altitude/slope/aspect gradients) as well as the seasonal range of variation at different time scales and their annual variability. This estimation may provide a first estimate of the order of magnitude of uncertainty of average calculations or spatial interpolation from a scarce number of weather stations in Mediterranean and semiarid mountain areas.

The correct assessment of the solar radiation regime is crucial to correctly determine the temporal evolution of energy-limited hydrological processes such as the snow layer dynamics, soil moisture depletion and evapotranspiration (Tomas-Burguera et al., 2019). Thus, as a key input parameter for the water and energy balance, these high spatial resolution solar radiation time series are useful not only for research on the snow domain and water planning in SN in the application of hydrological

modelling, but in many other applications. For example, within the agricultural sector in the estimations of evapotranspiration for irrigation scheduling, ecology and biodiversity studies, stand-alone solar energy facilities designing and location, recreational activities in the area that strongly rely on the hydro-meteorological conditions of SN, etc.. Finally, this work contributes to feed research related to some key questions in hydrology, as UPH 16 and UPH 5 identified by Blöschl et al. (2019).

#### Author contributions

CA, in collaboration with MJP, conceived the research. CA processed the data, applied the quality control to the raw global radiation data, modelled global radiation datasets and developed the cross-validation algorithms. RP processed satellite data, generated albedo maps for the study period, prepared the final figures and the available datasets generated in the study. CA prepared the manuscript with contributions of MJP and RP; all authors discussed and revised the final text.

#### Competing interests

The authors declare that they have no conflict of interest.

#### Acknowledgements

This study was supported by the following research projects funded by Spanish Ministry of Science and Innovation - MICINN: Research Project RTI2018-099043-B-I00, “Operability in hydrological management under snow torrentiality/drought conditions in high mountain in semiarid watersheds”; and, by Spanish Ministry of Economy and Competitiveness - MINECO: Research Project CGL 2014-58508R, “Global monitoring system for snow areas in Mediterranean regions: trends analysis and implications for water resource management in Sierra Nevada”, and Research Project CGL 2011-25632, “Snow dynamics in Mediterranean regions and its modelling at different scales. Implication for water management”. Moreover, the present work was partially developed within the framework of the Panta Rhei Research Initiative of the International Association of Hydrological Sciences (IAHS) (Working Groups Water and energy fluxes in a changing environment and Mountain Hydrology). Rafael Pimentel acknowledges fundings by the modality 5.2 of the *Programa Propio-2018* of the University of Cordoba and the *Juan de la Cierva Incorporación* Programme of the Ministry of Science and Innovation (IJC2018-038093-I). The continuous support of the Natural and National Park of Sierra Nevada has also been determinant for the development of this line of research since 2002. Finally, tremendous appreciation is extended to all the weather station networks that maintain and make accessible datasets to scientific research.

#### References

Aguilar, C. and Polo, M. J.: Generating reference evapotranspiration surfaces from the Hargreaves equation at watershed scale, Hydrol. Earth Syst. Sci., 15, 2495-2508, <https://doi.org/10.5194/hess-15-2495-2011>, 2011.



442 Aguilar, C., Herrero, J., and Polo, M. J.: Topographic effects on solar radiation distribution in mountainous watersheds and  
 443 their influence on reference evapotranspiration estimates at watershed scale, *Hydrol. Earth Syst. Sci.*, 14, 2479–2494,  
 444 <https://doi.org/10.5194/hess-14-2479-2010>, 2010.

445 Aguilar, C., Pimentel, R., and Polo, M. J.: Time series of distributed global radiation data in Sierra Nevada (Spain) at different  
 446 scales from historical weather stations, *PANGAEA*, <https://doi.pangaea.de/10.1594/PANGAEA.921012>, 2021.

447 Allen, R.G.: Self-calibrating method for estimating solar radiation from air temperature, *J. Hydrol. Eng.*, 2, 56-67,  
 448 [https://doi.org/10.1061/\(ASCE\)1084-0699\(1997\)2:2\(56\)](https://doi.org/10.1061/(ASCE)1084-0699(1997)2:2(56)), 1997.

449 Anderson, R. S., Jiménez-Moreno, G., Carrión, J. S., and Pérez-Martínez, C.: Postglacial history of alpine vegetation, fire, and  
 450 climate from Laguna de Río Seco, Sierra Nevada, southern Spain, *Quaternary Sci. Rev.*, 30, 1615–1629,  
 451 <https://doi.org/10.1016/j.quascirev.2011.03.005>, 2011.

452 Batllés, J., Bosch, J.L., Tovar-Pescador, J., Martínez-Durbán, M., Ortega, R., and Miralles, I.: Determination of atmospheric  
 453 parameters to estimate global radiation in areas of complex topography: Generation of global irradiation map, *Energy Convers.*  
 454 *Manage.*, 49, 336-345, <https://doi.org/10.1016/j.enconman.2007.06.012>, 2008.

455 Bechini, L., Ducco, G., Donatelli, M. and Stein, A.: Modelling, interpolation and stochastic simulation in space and time of  
 456 global solar radiation, *Agric. Ecosyst. Environ.*, 81, 29-42, [https://doi.org/10.1016/S0167-8809\(00\)00170-5](https://doi.org/10.1016/S0167-8809(00)00170-5), 2000.

457 Blanca, G., Cueto, M., Martínez-Lirola, M. J., and Molero-Mesa, J.: Threatened vascular flora of Sierra Nevada (Southern  
 458 Spain), *Biological Conservation*, 85(3), 269-285, doi:10.1016/S0006-3207(97)00169-9, 1998.

459 Blöschl, G. et al.: Twenty-three unsolved problems in hydrology (UPH) – a community perspective, *Hydrol. Sci. J.*, 64 (1),  
 460 1141-1158, <https://doi.org/10.1080/02626667.2019.1620507>, 2019.

461 Bonet-García, F.J., Pérez-Luque, A.J., Moreno-Llorca, R.A., Pérez-Pérez, R., Puerta-Piñero, C., and Zamora, R.: Protected  
 462 areas as elicitors of human well-being in a developed region: a new synthetic (socioeconomic) approach, *Biol. Conserv.*, 187  
 463 221-9, <https://doi.org/10.1016/j.biocon.2015.04.027>, 2015.

464 Bosch, J.L., López, G., and Batllés, F.J.: Daily solar irradiation estimation over a mountainous area using artificial neural  
 465 networks, *Renew. Energy*, 33, 1622-1628, <https://doi.org/10.1016/j.renene.2007.09.012>, 2008.

466 Brest, C.L. and Goward, S.N.: Deriving surface albedo measurements from narrow band satellite data, *Int. J. Remote Sens.*,  
 467 8, 351-367, <https://doi.org/10.1080/01431168708948646>, 1987.

468 Bristow, K.L. and Campbell, G.S.: On the relationship between incoming solar radiation and daily maximum and minimum  
 469 temperature, *Agric. For. Meteorol.*, 31, 159-166, [https://doi.org/10.1016/0168-1923\(84\)90017-0](https://doi.org/10.1016/0168-1923(84)90017-0), 1984.

470 Cañadas, E. M., Fenu, G., Peñas, J., Lorite, J., Mattana, E., and Bacchetta, G.: Hotspots within hotspots: 445 Endemic plant  
 471 richness, environmental drivers, and implications for conservation, *Biological Conservation*, 170, 282-291,  
 472 <https://doi.org/10.1016/j.biocon.2013.12.007>, 2014.

473 Chen, J.M., Liu, J., Cihlar, J., and Goulden, M.L.: Daily canopy photosynthesis model through temporal and spatial scaling  
 474 for remote sensing applications, *Ecol. Modell.*, 124, 99-119, [https://doi.org/10.1016/S0304-3800\(99\)00156-8](https://doi.org/10.1016/S0304-3800(99)00156-8), 1999.

475 Chen, X., Su, Z., Ma, Y., Yang, K., and Wang, B.: Estimation of surface energy fluxes under complex terrain of Mt.  
 476 Qomolangma over the Tibetan Plateau, *Hydrol. Earth Syst. Sci.*, 17, 1607-1618, <https://doi.org/10.5194/hess-17-1607-2013>,  
 477 2013.

478 Diodato, N. and Bellocchi, G.: Modelling solar radiation over complex terrains using monthly climatological data, *Agric. For.*  
 479 *Meteorol.* 144, 111-126, <https://doi.org/10.1016/j.agrformet.2007.02.001>, 2007.

480 Donatelli, M., Bellocchi, G., and Fontana, F.: RadEst3.00: software to estimate daily radiation data from commonly available  
 481 meteorological variables, *European J. Agron.*, 18, 363-367, [https://doi.org/10.1016/S1161-0301\(02\)00130-2](https://doi.org/10.1016/S1161-0301(02)00130-2), 2003.

482 Donatelli, M., Carlini, L., and Bellocchi, G.: A software component for estimating solar radiation, *Environ. Modell. Software*,  
 483 21(3), 411-416, <https://doi.org/10.1016/j.envsoft.2005.04.002>, 2006.

484 Dozier, J. and Frew, J.: Rapid calculation of terrain parameters for radiation modeling from digital elevation data, *IEEE Trans.*  
 485 *Geosci. Remote Sens.*, 28, 963-969, <https://doi.org/10.1109/36.58986>, 1990.

486 Dozier, J., Bruno, J., and Downey, P.: A faster solution to the horizon problem, *Comp. Geosci.*, 7, 145-151,  
 487 [https://doi.org/10.1016/0098-3004\(81\)90026-1](https://doi.org/10.1016/0098-3004(81)90026-1), 1981.

488 Dubayah, R.C.: Estimating net solar radiation using Landsat Thematic Mapper and digital elevation data, *Water Resour. Res.*,  
 489 28, 2469-2484, <https://doi.org/10.1029/92WR00772>, 1992.

490 Dubayah, R.C.: Modeling a solar radiation topo climatology for the Rio Grande river watershed, *J. Veg. Sci.* 5, 627-640,  
 491 <https://doi.org/10.2307/3235879>, 1994.

492 Dubayah, R.C. and van Katwijk, V.: The topographic distribution of annual incoming solar radiation in the Rio Grande river  
 493 basin, *Geophys. Res. Lett.*, 19(22), 2231-2234, <https://doi.org/10.1029/92GL02284>, 1992.

494 Dubayah, R. and Rich, P.M.: Topographic solar radiation models for GIS, *Int. J. Geogr. Inf. Syst.*, 9, 405-413,  
 495 <https://doi.org/10.1080/02693799508902046>, 1995.

496 El Ouderni, A.R., Maatallah, T., El Alimi, S., and Ben Nassrallah, S.: Experimental assessment of the solar energy potential  
 497 in the gulf of Tunis, Tunisia, *Renew. Sustain. Energy Rev.*, 20, 155-168, <https://doi.org/10.1016/j.rser.2012.11.016>, 2013.

498 Fu, P. and Rich, P.M.: A geometric solar radiation model and its applications in agriculture and forestry. In: *Proceedings of*  
 499 *the Second International Conference on Geospatial Information in Agriculture and Forestry*, Lake Buena Vista, 10-12 January  
 500 2000, I-357-364, 2000a.

501 Fu, P. and Rich, P.M.: The Solar Analyst 1.0 Manual. Helios Environmental Modeling Institute (HEMI), USA, 2000b.

502 Fu, P. and Rich, P.M.: A Geometric Solar Radiation Model with Applications in Agriculture and Forestry, *Comput. Electr.*  
 503 *Agric.*, 37, 25-35, [https://doi.org/10.1016/S0168-1699\(02\)00115-1](https://doi.org/10.1016/S0168-1699(02)00115-1), 2002.

504 Geiger, M., Diabate, L., Menard, L., and Wald, L.: A web service for controlling the quality of measurements of global solar  
 505 irradiation, *Sol. Energy*, 73, 474-480, [https://doi.org/10.1016/S0038-092X\(02\)00121-4](https://doi.org/10.1016/S0038-092X(02)00121-4), 2002.

506 Goldberg, V. and Häntzschel, J.: Application of a radiation model for small-scale complex terrain in a GIS environment,  
 507 *Meteorol. Zeitschrift*. 11(2), 119-128, <https://doi.org/10.1127/0941-2948/2002/0011-0119>, 2002.

508 Hargreaves, G.H. and Samani, Z.A.: Estimating potential evapotranspiration, *J. Irrig. Drain. Engin.* 108 IR3, 223-230, 1982.



509 Herrero, J. and Polo, M. J.: Parameterization of atmospheric longwave emissivity in a mountainous site for all sky conditions,  
 510 Hydrol. Earth Syst. Sci., 16, 3139–3147, <https://doi.org/10.5194/hess-16-3139-2012>, 2012.

511 Herrero, J. and Polo, M. J.: Evapsublimation from the snow in the Mediterranean mountains of Sierra Nevada (Spain), The  
 512 Cryosphere, 10, 2981–2998, <https://doi.org/10.5194/tc-10-2981-2016>, 2016.

513 Herrero, J., Polo, M. J., Moñino, A., and Losada, M. A.: An energy balance snowmelt model in a Mediterranean site, J. Hydrol.,  
 514 371, 98–107, <https://doi.org/10.1016/j.jhydrol.2009.03.021>, 2009.

515 Hewitt, G.M.: Mediterranean Peninsulas: the evolution of hotspots. In: Zachos, F.E. and Habel, J.C. (eds), Biodiversity  
 516 hotspots: distribution and protection of conservation priority area, Springer, Berlin, pp. 123-147, 2011.

517 Heywood, V. H.: The Mediterranean flora in the context of world diversity, Ecología Mediterránea, 21, 11-18, 1995.

518 Ineichen, P. and Pérez, R.: A new airmass independent formulation for the Linke Turbidity coefficient, Sol. Energy, 73, 151-  
 519 157, [https://doi.org/10.1016/S0038-092X\(02\)00045-2](https://doi.org/10.1016/S0038-092X(02)00045-2), 2002.

520 Iqbal, M.: An introduction to solar radiation, Academic Press, Ontario, 1983.

521 Jacovides, C.P., Hadjioannou, L., Pashiardis, S., and Stefanou, L.: On the diffuse fraction of daily and monthly global radiation  
 522 for the island of Cyprus, Sol. Energy, 56, 565-572, [https://doi.org/10.1016/0038-092X\(96\)81162-5](https://doi.org/10.1016/0038-092X(96)81162-5), 1996.

523 Journée, M. and Bertrand, C.: Quality control of solar radiation data within the RMIB solar measurements network, Sol.  
 524 Energy, 85, 72-86, <https://doi.org/10.1016/j.solener.2010.10.021>, 2011.

525 Kasten, F. and Young, A.T.: Revised optical air mass tables and approximation formula, App. Optics, 28(22), 4735-4738,  
 526 <https://doi.org/10.1364/AO.28.004735>, 1989.

527 Liu, M., Bárdossy, A., Li, J., and Jiang, Y.: GIS-based modelling of topography-induced solar radiation variability in complex  
 528 terrain for data sparse region, Int. J. Geogr. Inf. Sci., 26(7), 1281-1308, <https://doi.org/10.1080/13658816.2011.641969>, 2012a.

529 Liu, J.D., Liu, J.M., Linderholm, H.W., Chen, D.L., Yu, Q., Wu, D.R., and Haginoya, S.: Observation and calculation of the  
 530 solar radiation on the Tibetan Plateau, Energy Convers. Manag., 57, 23-32, <https://doi.org/10.1016/j.enconman.2011.12.007>,  
 531 2012b.

532 Liu, Y., Zhang, P., Nie, L., Xu, J., Lu, X., and Li, S.: Exploration of the Snow Ablation Process in the Semiarid Region in  
 533 China by Combining Site-Based Measurements and the Utah Energy Balance Model-A Case Study of the Manas River Basin,  
 534 Water, 11, 1058, <https://doi.org/10.3390/w11051058>, 2019

535 MacDonell, S., Kinnard, C., Mölg, T., Nicholson, L., and Abermann, J.: Meteorological drivers of ablation processes on a cold  
 536 glacier in the semi-arid Andes of Chile, The Cryosphere, 7, 1513–1526, <https://doi.org/10.5194/tc-7-1513-2013>, 2013.

537 Mamassis, N., Efstratiadis, A., and Apostolidou, I.G.: Topography-adjusted solar radiation indices and their importance in  
 538 hydrology, Hydr. Sc. J., 57(4), 756-775, <https://doi.org/10.1080/02626667.2012.670703>, 2012.

539 Martínez-Durbán, M., Zarzalejo, L.F., Bosch, J.L., Rosiek, S., Polo, J., and Batlles, F.J.: Estimation of global daily irradiation  
 540 in complex topography zones using digital elevation models and meteosat images: Comparison of the results, Energy Convers.  
 541 Manage. 50, 2233-2238, <https://doi.org/10.1016/j.enconman.2009.05.009>, 2009.

542 Moradi, I.: Quality control of global solar radiation using sunshine duration hours, *Energy*, 34, 1-6,  
 543 <https://doi.org/10.1016/j.energy.2008.09.006>, 2009.

544 Mullen, R., Marshall, L., and McGlynn, B.: A Beta Regression Model for Improved Solar Radiation Predictions, *J. Appl.*  
 545 *Meteor. Climatol.*, 52, 1923-1938, <https://doi.org/10.1175/JAMC-D-12-038.1>, 2013.

546 Muneer, T., Younes, S., and Munawwar, S.: Discourses on solar radiation, *Renew. Sust. Energy Rev.*, 11, 551-602,  
 547 <https://doi.org/10.1016/j.rser.2005.05.006>, 2007.

548 Myers, N., Mittermeier, R.A., Mittermeier, C.G., da Fonseca, G.A.B., and Kent, J.: Biodiversity hotspots for conservation  
 549 priorities, *Nature*, 403, 853-858, <https://doi.org/10.1038/35002501>, 2000.

550 O'Farrell, P.J., Reyers, B., Le Maitre, D.C., et al.: Multi-functional landscapes in semi arid environments: implications for  
 551 biodiversity and ecosystem services, *Landscape Ecol.*, 25, 1231-1246, <https://doi.org/10.1007/s10980-010-9495-9>, 2010.

552 Oliphant, A.J., Spronken-Smith, R.A., Sturman, A.P., and Owens, I.F.: Spatial Variability of Surface Radiation Fluxes in  
 553 Mountainous Terrain, *J. App. Meteorol.*, 42, 113-128, [https://doi.org/10.1175/1520-0450\(2003\)042<0113:SVOSRF>2.0.CO;2](https://doi.org/10.1175/1520-0450(2003)042<0113:SVOSRF>2.0.CO;2), 2003.

555 Pauli, H. et al.: Recent plant diversity changes on Europe's mountain summits, *Science* 336, 353-355,  
 556 <https://doi.org/10.1126/science.1219033>, 2012.

557 Pérez-Palazón, M. J., Pimentel, R., Herrero, J., Aguilar, C., Perales, J. M., and Polo, M. J.: Extreme values of snow-related  
 558 variables in Mediterranean regions: trends and long-term forecasting in Sierra Nevada (Spain), *Proc. IAHS*, 369, 157–162,  
 559 <https://doi.org/10.5194/piahs-369-157-2015>, 2015.

560 Pérez-Palazón, M. J., Pimentel, R., and Polo, M. J.: Climate Trends Impact on the Snowfall Regime in Mediterranean Mountain  
 561 Areas: Future Scenario Assessment in Sierra Nevada (Spain), *Water*, 10, 720, <https://doi.org/10.3390/w10060720>, 2018.

562 Pimentel, R., Herrero, J., and Polo, M.J.: Estimating snow albedo patterns in a Mediterranean site from Landsat TM and ETM+  
 563 images, In: *Proceedings of the SPIE, Remote Sensing for Agriculture, Ecosystems, and Hydrology XV*, 88870L, Dresden,  
 564 Germany, 23-26 September 2013, doi:10.1117/12.2029064.

565 Pimentel, R., Herrero, J., and Polo, M.J.: Graphic user interface to preprocess Landsat TM, ETM+ and OLI images for  
 566 hydrological applications. In: *Proceedings of the HIC 2014, 11th International Conference on Hydroinformatics*, New York,  
 567 17-21 August 2014.

568 Polo, M. J., Herrero, J., Pimentel, R., and Pérez-Palazón, M. J.: The Guadalfeo Monitoring Network (Sierra Nevada, Spain):  
 569 14 years of measurements to understand the complexity of snow dynamics in semiarid regions, *Earth Syst. Sci. Data*, 11, 393–  
 570 407, <https://doi.org/10.5194/essd-11-393-2019>, 2019.

571 Ruiz-Arias, J.A., Tovar-Pescador, J., Pozo-Vázquez, D., and Alsamamra, H.: A comparative analysis of DEM-based models  
 572 to estimate the solar radiation in mountainous terrain, *Int. J. Geogr. Inf. Sci.*, 23, 1049-1076,  
 573 <https://doi.org/10.1080/13658810802022806>, 2009.

574 Ruiz-Arias, J.A., Alsamamra, H., Tovar-Pescador, J., and Pozo-Vázquez, D.: Proposal of a regressive model for the hourly  
575 diffuse solar radiation under all sky conditions, *Energy Convers. Manage.*, 51, 881-893,  
576 <https://doi.org/10.1016/j.enconman.2009.11.024>, 2010.

577 Ruiz-Arias, J.A., Pozo-Vázquez, D., Santos-Alamillos, F.J., Lara-Fanego, V., and Tovar-Pescador, J.A.: Topographic  
578 geostatistical approach for mapping monthly mean values of daily global solar radiation: A case study in southern Spain, *Agric.*  
579 *For. Meteorol.*, 151, 1812-1822, <https://doi.org/10.1016/j.agrformet.2011.07.021>, 2011.

580 Scaffetta, N. and Willson, R.C.: Multiscale comparative spectral analysis of satellite total solar irradiance measurements from  
581 2003 to 2013 reveals a planetary modulation of solar activity and its nonlinear dependence on the 11 yr solar cycle, *Pattern*  
582 *Recogn. Phys.*, 1, 123-133, doi: 10.5194/prp-1-123-2013, 2013.

583 Sheng, J., Wilson, J.P., and Lee, S.: Comparison of land surface temperature (LST) modeled with a spatially-distributed solar  
584 radiation model (SRAD) and remote sensing data, *Environ. Modell. Software*, 24(3), 436-443,  
585 <https://doi.org/10.1016/j.envsoft.2008.09.003>, 2009.

586 Šuri, M. and Hofierka, J.: A new GIS-based solar radiation model and its application to photovoltaic assessments, *Trans. GIS*,  
587 8(2), 175-190, <https://doi.org/10.1111/j.1467-9671.2004.00174.x>, 2004.

588 Tang, W., Yang, K., Qin, J., Li, X., and Niu, X.: A 16-year dataset (2000–2015) of high-resolution (3 h, 10 km) global surface  
589 solar radiation, *Earth Syst. Sci. Data*, 11, 1905–1915, <https://doi.org/10.5194/essd-11-1905-2019>, 2019.

590 Tomas-Burguera, M., Vicente-Serrano, S. M., Beguería, S., Reig, F., and Latorre, B.: Reference crop evapotranspiration  
591 database in Spain (1961–2014), *Earth Syst. Sci. Data*, 11, 1917–1930, <https://doi.org/10.5194/essd-11-1917-2019>, 2019.

592 Tovar, J., Olmo, F.J., and Alados-Arboledas, L.: Local scale variability of solar radiation in a mountainous region, *J. App.*  
593 *Meteorol.*, 34, 2316-2322, [https://doi.org/10.1175/1520-0450\(1995\)034<2316:LSVOSR>2.0.CO;2](https://doi.org/10.1175/1520-0450(1995)034<2316:LSVOSR>2.0.CO;2), 1995.

594 Tovar-Pescador, J., Pozo-Vázquez, D., Ruiz-Arias, J.A., Batllés, J., López, G., and Bosch, J.L.: On the use of the digital  
595 elevation model to estimate the solar radiation in areas of complex terrain, *Meteorol. Appl.*, 13, 279-287,  
596 <https://doi.org/10.1017/S1350482706002258>, 2006.

597 Wilson, J.P. and Gallant, J.C.: Secondary topographic attributes. In: Wilson, J.P. and Gallant, J.C. (eds), *Terrain Analysis:*  
598 *Principles and Applications*, John Wiley & Sons, New York, pp. 51-85, 2000.

599 Winslow, J.C., Hunt, E.R., and Piper, S.C.: A globally applicable model of daily solar irradiance estimated from air temperature  
600 and precipitation data, *Ecol. Modell.*, 143, 227-243, [https://doi.org/10.1016/S0304-3800\(01\)00341-6](https://doi.org/10.1016/S0304-3800(01)00341-6), 2001.

601 Wu, G.F., Liu, Y.L., and Wang, T.J.: Methods and strategy for modeling daily global solar radiation with measured  
602 meteorological data-A case study in Nanchang station, China, *Energy Convers. Manage.*, 48, 2447-2452,  
603 <https://doi.org/10.1016/j.enconman.2007.04.011>, 2007.

604 Yang, K. and Koike, T.: A general model to estimate hourly and daily solar radiation for hydrological studies., *Water Resour.*  
605 *Res.* 41(10), W10403, doi: 10.1029/2005WR003976, <https://doi.org/10.1029/2005WR003976>, 2005.

606 Yang, K., Koike, T., and Ye, B.: Improving estimation of hourly, daily, and monthly solar radiation by importing global data  
607 sets, *Agric. For. Meteorol.*, 137, 43-55, <https://doi.org/10.1016/j.agrformet.2006.02.001>, 2006.

608 Yang, K., He, J., Tang, W.J., and Qin, J. and Cheng, C.C.K.: On downward shortwave and longwave radiations over high  
609 altitude regions: Observation and modeling in the Tibetan Plateau, *Agric. For. Meteorol.*, 150, 38-46,  
610 <https://doi.org/10.1016/j.agrformet.2009.08.004>, 2010.

611 Yang, L., Cao, Q., Yu, Y., and Liu, Y.: Comparison of daily diffuse radiation models in regions of China without solar radiation  
612 measurement, *Energy*, 191, 116571, <https://doi.org/10.1016/j.energy.2019.116571>, 2020.

613 Younes, S., Claywell, R., and Muneer, T.: Quality control of solar radiation data: present status and proposed new approaches,  
614 *Energy*, 30, 1533-1549, <https://doi.org/10.1016/j.energy.2004.04.031>, 2005.

615 Zhang, S., Li, X., She, J., and Peng, X. 2019. Assimilating remote sensing data into GIS-based all sky solar radiation modeling  
616 for mountain terrain, *Remote Sens. Envir.*, 231, <https://doi.org/10.1016/j.rse.2019.111239>, 2019.

617 Zhang, M., Wang, B., Liu, D.L., Liu, J., Zhang, H., Feng, P., Kong, D., Cleverly, J., Yang, X., and Yu, Q.: Incorporating  
618 dynamic factors for improving a GIS-based solar radiation model. *Trans. GIS* 2020, <https://doi.org/10.1111/tgis.12607>, 2020.

## 620 **Appendix A. Solar radiation equations**

621 The sequence followed by the model is summarized in Figure A1. Computations are classified at the point scale of weather  
622 stations (Point) and the distributed scale of grids of the Digital Elevation Model (DEM) (Distributed). The complete  
623 explanation of the algorithms and assumptions of the model can be found in detail in Aguilar et al. (2010).

624 Firstly, daily extraterrestrial radiation ( $R_{ext}$  in  $\text{MJ m}^{-2} \text{ day}^{-1}$ ) is computed by integrating the extraterrestrial radiation incident  
625 upon a horizontal surface relative to the sun's beams from sunrise to sunset (Eq. A1).

$$626 \quad R_{ext} = E_o \cdot I_{SC} \cdot \cos(\theta_z) \quad (A1)$$

627 where  $I_{SC}$  is the solar constant ( $1367 \text{ W m}^{-2}$ ),  $\theta_z$  is the zenith angle and  $E_o$ , the eccentricity factor. These variables were  
628 computed following the equations in Dozier et al. (1981).

629 Then, the daily clearness index (CI), as the ratio of observed daily global radiation ( $R_{go}$  in  $\text{MJ m}^{-2} \text{ day}^{-1}$ ) to the daily  
630 extraterrestrial radiation, is computed at each weather station (Eq. A2).

$$631 \quad CI = \frac{R_{go}}{R_{ext}} \quad (A2)$$

632 CI is expressed in terms of two factors,  $CI_{CS}$  and  $fCI_{cl}$ . The first term represents the influence of atmosphere under clear-sky  
633 conditions over solar radiation, while the second term includes the cloudiness effects that decrease the final incoming solar  
634 radiation (Eq. A3). The approximation of Ineichen and Perez (2002) is used to compute the global radiation under clear-sky  
635 conditions,  $R_{gcs}$ , and thus, distributed hourly  $R_{gcs}$  values are obtained from the sun elevation angle, the height of the cell, the  
636 Linke turbidity factor ( $T_L$ ) and the atmospheric mass obtained following the parameterization of Kasten and Young (1989).

Thus, hourly  $CI_{CS}$  values can be computed cell by cell and then the mean daily distributed values are generated. Once daily  $CI$  and  $CI_{CS}$  values are known,  $fCI_{cl}$  is obtained at each weather station from Eq. A3 and spatially interpolated following the inverse distance weighted (IDW) method. From daily  $CI_{CS}$  and  $fCI_{cl}$  maps, daily interpolated  $CI$  and  $R_g$  values can be obtained at cell scale from Eq. A3 and A4.

$$CI = CI_{CS} \cdot fCI_{cl} \quad (A3)$$

$$R_g = R_{ext} \cdot CI_{CS} \cdot fCI_{cl} \quad (A4)$$

Topographic effects need to be evaluated for the different sun positions during the day and thus, hourly values of the different components need to be derived. Two different procedures are currently available in the model. The first one proposed in Aguilar et al. (2010) applies Jacovides et al. (1996) (Eq. A5.1) to produce the daily diffuse ( $R_d$  in  $MJ\ m^{-2}\ day^{-1}$ ) and daily beam values ( $R_b$  in  $MJ\ m^{-2}\ day^{-1}$ ). The model finally computes hourly beam and diffuse values on horizontal surfaces ( $r_b$  and  $r_d$ , both in  $MJ\ m^{-2}\ h^{-1}$ ), from the daily amounts and following the temporal pattern of extraterrestrial hourly radiation during the day.

$$\frac{R_d}{R_g} = \begin{cases} 0.992 - 0.0486CI & CI \leq 0.1 \\ 0.954 + 0.734CI - 3.806CI^2 + 1.703CI^3 & 0.1 < CI \leq 0.71 \\ 0.165 & CI > 0.71 \end{cases} \quad (A5.1)$$

The second approach uses the temporal pattern of extraterrestrial hourly radiation,  $r_{ext}$ , to generate hourly global values,  $r_g$  according to previous studies (Chen et al., 1999; Ruiz-Arias et al., 2011). Then, the hourly regressive model developed by Ruiz-Arias et al. (2010) is applied to estimate the hourly diffuse values (Eq. A5.2) from the hourly  $CI$ ,  $CI_h$ , as the ratio of  $r_g$  to  $r_{ext}$ . This model was implemented as it has been validated over Europe and USA using ground data from different sites, including some Spanish stations (Ruiz-Arias et al., 2010). Hourly beam values ( $r_b$ ) are thus obtained on a cell basis as the difference between global and diffuse hourly radiation distributed values.

$$\frac{r_d}{r_g} = 0.952 - 1.041e^{-\exp(2.3-4.702 \cdot CI_h)} \quad (A5.2)$$

First applications at the study site have shown negligible differences between both partitioning schemes. The differences with daily recorded data were insignificant in the second decimal place of error values. Thus, the results presented in this study were obtained with the original scheme of Aguilar et al. (2010) (Eq. A5.1) while the authors continue working on the improvement on the partitioning scheme of the model.

Then, the topographic correction is carried out and depending on the component, different procedures are applied.

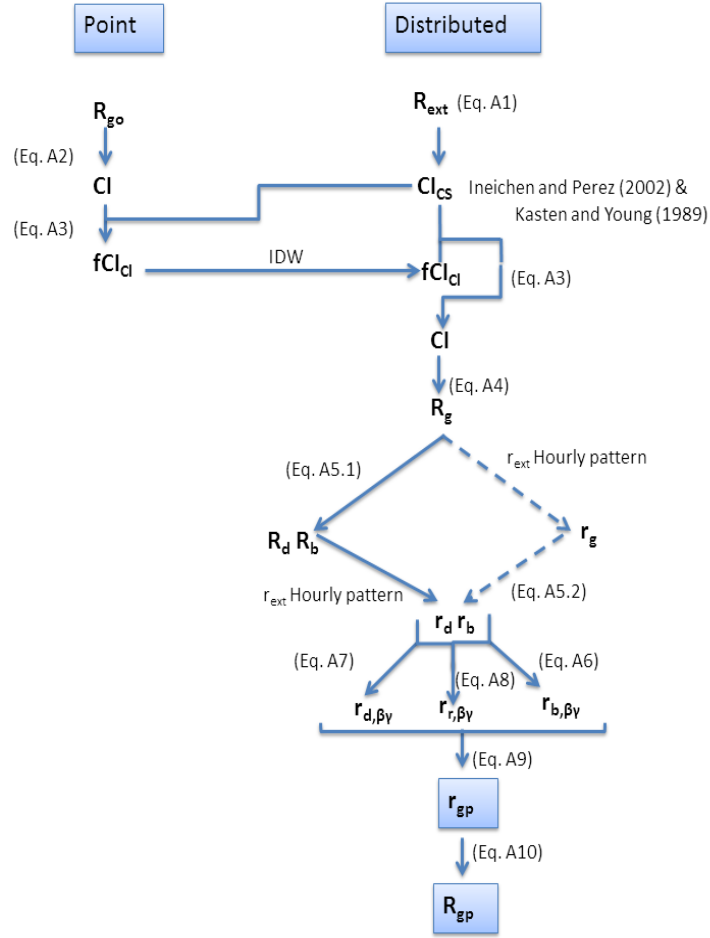


**Figure A1. Flow chart of the solar radiation model**

Hourly beam radiation on a surface of slope  $\beta$  and orientation  $\gamma$ , ( $r_{b,\beta\gamma}$  in  $\text{MJ m}^{-2} \text{h}^{-1}$ ), is calculated according to Eq. A6. in terms of  $r_b$ ,  $\theta_z$  and a new corrected zenith angle for the sloping surface,  $\theta$  (Iqbal, 1983). Then, the model checks the shading effects. Self-shading will occur if the angle between the normal to the surface and the solar vector is greater than 90 degrees. Finally, shading by nearby terrain takes place when the illumination angle is greater than the horizon angle in the same direction. The model previously obtains the horizons following the algorithms of Dozier et al. (1981) and Dozier and Frew (1990), by comparing the slopes between cells in the eight directions.

$$r_{b,\beta\gamma} = r_b \left( \frac{\cos \theta}{\cos \theta_z} \right) \quad (\text{A6})$$

Hourly diffuse radiation on a surface of slope  $\beta$  and orientation  $\gamma$  ( $r_{d,\beta\gamma}$  in  $\text{MJ m}^{-2} \text{h}^{-1}$ ), is calculated according to Eq. A7 in terms of  $r_d$  and SVF, the sky view factor, that modifies the incoming radiation incident on a flat surface to consider possibly obstruction effects on a sloping surface (Dubayah, 1992). Dozier and Frew (1990) obtained an analytical expression for the estimation of the SVF in terms of the different horizons in each direction considered assuming an isotropic sky.

$$r_{d,\beta\gamma} = r_d \cdot SVF \quad (\text{A7})$$

Finally, hourly reflected radiation on a surface of slope  $\beta$  and orientation  $\gamma$  ( $r_{r,\beta\gamma}$  in  $\text{MJ m}^{-2} \text{h}^{-1}$ ) and albedo  $\rho$  is calculated according to Dozier and Frew (1990) as expressed in Eq. A8.

$$r_{r,\beta\gamma} = \rho \cdot \left[ \frac{1 + \cos \beta}{2} - SVF \right] \cdot (r_d + r_b) \quad (\text{A8})$$

Hourly global distributed radiation ( $r_{gp}$  in  $\text{MJ m}^{-2} \text{h}^{-1}$ ) is obtained by addition of the three hourly components at each cell according to Eq. A9.

$$r_{gp} = r_{b,\beta\gamma} + r_{d,\beta\gamma} + r_{r,\beta\gamma} \quad (\text{A9})$$

Finally, daily global distributed radiation ( $R_{gp}$  in  $\text{MJ m}^{-2} \text{day}^{-1}$ ) is obtained as the summation of hourly global distributed radiation values (Eq. A10).

$$R_{gp} = \sum_{24h} r_{gp} \quad (\text{A10})$$

## Appendix B: Comparison with Solar Analyst estimates

Solar Analyst (SA) is one of the most used GIS-based solar radiation models. It calculates the insolation across a landscape or for specific locations, based on the methods developed by Fu and Rich (2000a, 2000b, 2002). The total amount of radiation is given as global radiation and depends on the latitude of the site, topography, shadow cast and atmospheric attenuation. Global radiation is computed in SA as the sum of direct and diffuse radiation. The equations and modeling scheme can be found in detail in Fu and Rich (2000b).

Daily global radiation time series were generated in the study site with the Points Solar Radiation tool of SA at each weather station. Then a cross validation on a leave-one-out process was applied. The main inputs to the model, the diffuse fraction,  $k$ , and the atmospheric transmittivity,  $\tau$ , were estimated in the study site from observed global radiation data following Batlles et al. (2008).

SA underestimated observed daily values with a mean  $\alpha$  value of 0.78 in the global datasets (Table B.1). In general, worse approximations to observed data than those shown in Figure 4 were obtained with mean  $r^2$  values of 0.66 and RMSE values ranging from 3.59 (station 853) to 5.11 (station 859) with the global datasets (Table B.1). In terms of the cloudiness level, a general underestimation by SA was always seen on cloudy ( $CI \leq 0.3$ ) and clear-sky days ( $CI > 0.6$ ) with slopes of the fits

significantly lower than 1 (mean  $\alpha$  values of 0.42 and 0.74 respectively). In contrast, a slight overestimation with a mean  $\alpha$  value of 1.03 was found on partly cloudy days ( $0.3 < CI \leq 0.6$ ). As for RMSE values, the lowest mean values were always found for cloudy days ( $1.59 \text{ MJ m}^{-2} \text{ day}^{-1}$ ), also lower than those obtained in Figure 4 ( $3.70 \text{ MJ m}^{-2} \text{ day}^{-1}$ ). However, despite the lower RMSE values the deviation from the 1:1 linear fit in cloudy days with SA estimates was significant (mean  $\alpha$  value of 0.42 and  $r^2$  value of 0.39 in Table B.1). The highest RMSE values with SA estimates were always found on partly cloudy days with a mean value of  $5.35 \text{ MJ m}^{-2} \text{ day}^{-1}$  followed by clear-sky days with a mean RMSE value of  $3.37 \text{ MJ m}^{-2} \text{ day}^{-1}$ , both considerably higher than those obtained in subsection 3.4 ( $3.07$  and  $2.07 \text{ MJ m}^{-2} \text{ day}^{-1}$  respectively).

Table B.1. Model performance with Solar Analyst: slope ( $\alpha$ ) and  $r^2$  of the linear fit between daily predicted vs. observed  $R_g$  and RMSE ( $\text{MJ m}^{-2} \text{ day}^{-1}$ )

Station		Global data			CI≤0.3			0.3< CI≤0.6			CI>0.6		
z(m)	Code	$\alpha$	$r^2$	RMSE	$\alpha$	$r^2$	RMSE	$\alpha$	$r^2$	RMSE	$\alpha$	$r^2$	RMSE
781	602	0.77	0.69	4.05	0.27	0.43	1	0.96	0.33	5.44	0.74	0.8	3
942	608	0.73	0.74	3.78	0.23	0.46	1.06	0.86	0.54	4.56	0.7	0.81	2.97
950	601	0.73	0.73	3.74	0.3	0.38	1.12	0.9	0.53	4.47	0.7	0.79	3.2
975	853	0.74	0.76	3.59	0.23	0.27	1.02	0.92	0.6	4.27	0.71	0.82	2.86
1212	604	0.78	0.7	4.11	0.29	0.37	1.36	0.98	0.5	4.89	0.74	0.79	3.23
1332	803	0.75	0.71	4.07	0.38	0.5	1.27	0.99	0.46	4.89	0.72	0.8	3.2
1530	854	0.79	0.7	4.22	0.39	0.59	1.34	1	0.49	5.12	0.74	0.8	3.11
1732	857	0.85	0.61	4.84	0.43	0.39	1.69	1.1	0.23	6.23	0.8	0.74	3.38
1735	859	0.83	0.55	5.11	0.55	0.45	1.49	1.2	0.13	6.44	0.78	0.77	3.34
2141	804	0.67	0.68	4.02	0.24	0.17	0.95	0.97	0.5	4.72	0.64	0.79	3.21
2155	855	0.78	0.6	4.96	0.55	0.45	1.93	1.14	0.48	5.37	0.73	0.77	3.56
2300	858	0.65	0.62	4.69	0.54	0.39	2	0.87	0.41	5.55	0.61	0.69	4.07
2325	1002	0.81	0.54	4.98	0.61	0.51	2.15	1.17	0.14	6.23	0.76	0.7	3.64
2510	802	0.79	0.65	4.67	0.57	0.49	2.17	1.09	0.41	5.64	0.75	0.78	3.45
2867	1001	0.88	0.63	4.8	0.5	0.34	2.47	1.16	0.37	5.69	0.84	0.75	3.75
3097	860	0.85	0.6	4.95	0.58	0.08	2.45	1.22	0.24	6.1	0.81	0.74	3.87
Mean		0.78	0.66	4.41	0.42	0.39	1.59	1.03	0.40	5.35	0.74	0.77	3.37

## Appendix C: Nomenclature

### Symbols

CI: daily clearness index



713	$CI_{CS}$ : daily clearness index in a cloudless atmosphere
714	$CI_h$ : hourly clearness index
715	$E_o$ : eccentricity factor
716	$fCI_{cl}$ : cloudiness effects factor
717	$I_{SC}$ : solar constant
718	$k$ : diffuse to global irradiance ratio
719	$N_{CI<0.3}$ : rate of days for cloudy conditions
720	$N_{0.3<CI<0.6}$ : rate of days for partially cloudy conditions
721	$N_{CI>0.6}$ : rate of days for clear-sky conditions
722	$N_o$ : number of initially available daily records in the study period
723	$N$ : number of available daily records after the quality check
724	$Q_1$ : Quartile 1
725	$Q_3$ : Quartile 3
726	$R_b$ : daily beam radiation
727	$R_{bp}$ : daily beam radiation predicted by the model
728	$R_d$ : daily diffuse radiation
729	$R_{dp}$ : daily diffuse radiation predicted by the model
730	$R_{ext}$ : daily extraterrestrial radiation
731	$R_g$ : global radiation
732	$R_{gcs}$ : global radiation under clear-sky conditions
733	$R_{go\_max}$ : maximum daily global radiation observed value
734	$R_{go\_mean}$ : mean daily global radiation observed value
735	$R_{go\_min}$ : minimum daily global radiation observed value
736	$R_{gp}$ : daily global radiation predicted by the model
737	$r_b$ : hourly beam radiation on horizontal surfaces
738	$r_{b,\beta\gamma}$ : hourly beam radiation on a surface of slope $\beta$ and orientation $\gamma$
739	$r_d$ : hourly diffuse radiation on horizontal surfaces
740	$r_{d,\beta\gamma}$ : hourly diffuse radiation on a surface of slope $\beta$ and orientation $\gamma$
741	$r_{ext}$ : hourly extraterrestrial radiation
742	$r_{r,\beta\gamma}$ : hourly reflected radiation on a surface of slope $\beta$ and orientation $\gamma$
743	$r_g$ : hourly global radiation on horizontal surfaces
744	$r_{gp}$ : hourly global radiation predicted by the model
745	$R^2$ : coefficient of determination
746	$T_L$ : Linke turbidity factor

747 z: elevation

748

749 **Abbreviations**

750 DEM: Digital Elevation Model

751 IDW: Inverse Distance Weighted

752 RMSE: Root Mean Square Error

753 SA: Solar Analyst

754 SN: Sierra Nevada mountain range

755 SVF: Sky view factor

756 UPH: Unsolved Problems in Hydrology

757

758 **Greek symbols**

759  $\alpha$ : slope of the fit between  $R_{gp}$  and  $R_{go}$

760  $\beta$ : slope

761  $\gamma$ : orientation

762  $\mu_k$ : mean of the diffuse to global irradiance ratio

763  $\rho$ : albedo

764  $\sigma_k$ : standard deviation of the diffuse to global irradiance ratio

765  $\theta$ : corrected zenith angle for the sloping surface

766  $\theta_z$ : zenith angle

767